

STUDY OF FLOW INSIDE THERMOACOUSTIC SYSTEM

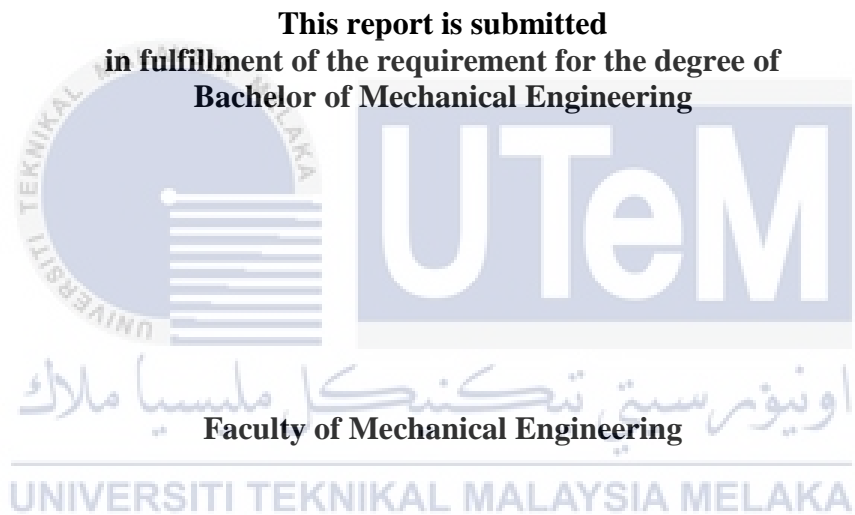


LEE WEE TECK

UNIVERSITI TEKNIKAL MALAYSIA MELAKA

STUDY OF FLOW INSIDE THERMOACOUSTIC SYSTEM

LEE WEE TECK



UNIVERSITI TEKNIKAL MALAYSIA MELAKA

2019

DECLARATION

I declare that this project report entitled “Study Of The Flow Inside Thermoacoustic System” is the result of my own work except as cited in the references.

Signature	:
Name	:	LEE WEE TECK
Date	:



اونيورسيتي تیکنیکل ملیسیا ملاک
UNIVERSITI TEKNIKAL MALAYSIA MELAKA

APPROVAL

I hereby declare that I have read this project report and in my opinion this report is enough in terms of scope and quality for the award of the degree of Bachelor of Mechanical Engineering.

Signature :

Supervisor Name : DR. FATIMAH AL-ZAHRAH BINTI MOHD SA'AT

Date :



UNIVERSITI TEKNIKAL MALAYSIA MELAKA

DEDICATION

To my beloved father and mother.



ABSTRACT

The study of flow in thermoacoustic system is important in order to find out ways to increase the efficiency of thermoacoustic engine. However, the study of thermoacoustic principle is difficult to be understood without the working experimental apparatus and simulation model. The objectives of this project is to design a small scale thermoacoustic prototype for experimentation, to test the small scale thermoacoustic system using suitable measurement methods, and to model a simple thermoacoustic flow field by using computational fluid dynamics (CFD) software. In experimentation, a small thermoacoustic refrigerator (TAR) rig that is operating under 133.45 Hz is built with two different type of stacks; acrylonitrile butadiene styrene (ABS) and stainless-steel scrubber. In CFD simulation, a simple CFD model is designed based on the actual operating parameters of the experiment rig with ABS stack only. Experimental result shows that a temperature drops of approximately 1 °C is achieved for both type of stacks and the same result is also obtained from the CFD simulation with ABS as the stack. The results are discussed and the recommendations for further research on the study of flow inside thermacoustic system are suggested at the end of the report.

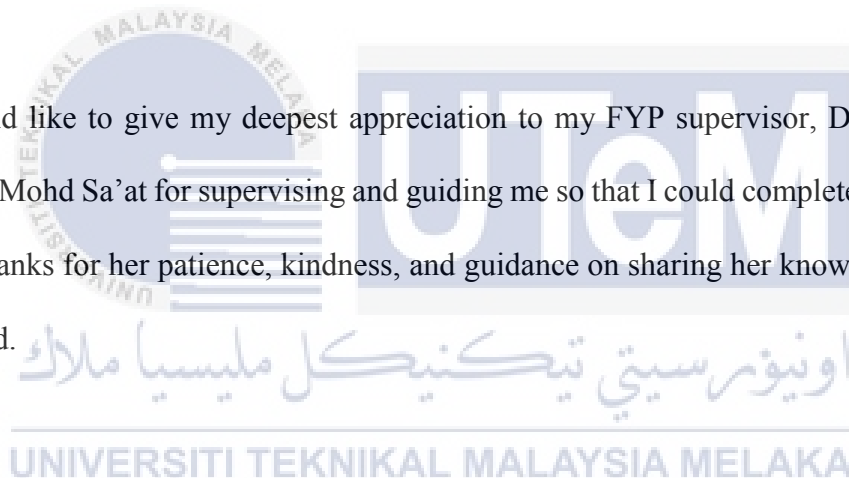
ABSTRAK

Kajian aliran dalam sistem termoakustik adalah penting untuk mengetahui cara meningkatkan kecekapan enjin termoakustik. Walau bagaimanapun, kajian prinsip termoakustik sukar difahami tanpa peralatan uji kaji dan model simulasi. Objektif projek ini adalah untuk merekabentuk prototaip termoakustik berskala kecil untuk eksperimen, untuk menguji sistem termoakustik berskala kecil dengan menggunakan kaedah pengukuran yang sesuai, dan memodelkan medan aliran termoakustik dengan menggunakan perisian dinamik bendalir komputasi (CFD). Dalam eksperimen, sebuah penyejuk termoakustik kecil (TAR) yang beroperasi di bawah 133.45 Hz dibina dengan menggunakan dua jenis timbunan yang berbeza yang diperbuat daripada acrylonitrile butadiene styrene (ABS) dan span keluli tahan karat dan diuji dengan menggunakan instrumen ukuran yang sesuai. Dalam simulasi CFD, satu model CFD yang mudah telah direka berdasarkan parameter operasi sebenar dalam rig uji kaji yang menggunakan timbunan ABS sahaja. Hasilnya, kejatuhan suhu adalah kira-kira 1 °C untuk kedua-dua jenis timbunan dapat dihasilkan dan keputusannya adalah sama dengan apa yang didapatkan daripada simulasi CFD untuk ABS sahaja. Semua dapatan dalam projek ini dibincangkan dan cadangan untuk penyelidikan lanjut tentang kajian aliran di dalam sistem termoakustik dicadangkan di bahagian hujung laporan.

ACKNOWLEDGEMENT

First and foremost, I would like to say thank you to Universiti Teknikal Malaysia Melaka (UTeM) for providing me a golden opportunity to study the Bachelor of Mechanical Engineering course and providing facilities, equipment, and resources to me in order to complete my final year project (FYP).

Next, I would like to give my deepest appreciation to my FYP supervisor, DR. Fatimah Al-Zahrah binti Mohd Sa'at for supervising and guiding me so that I could complete my FYP along this year. Thanks for her patience, kindness, and guidance on sharing her knowledge regarding my FYP field.



After that, I want to say thank you to my second examiner, DR. Mohamad Shukri bin Zakaria and Prof. Madya DR. Tee Boon Tuan for providing me suggestions and advices for my FYP. I would also like to thank Miss Dahlia binti Johari for her kindness to share her knowledge and experience on thermoacoustic and measurement instrumentation.

Lastly, I want to thank my coursemates, friends, and family for their encouragement and mental support throughout my study in UTeM.

TABLE OF CONTENT

CHAPTER	CONTENT	Page
	DECLARATION	i
	APPROVAL	ii
	DEDICATION	iii
	ABSTRACT	iv
	ABSTRAK	v
	ACKNOWLEDGEMENT	vi
	TABLE OF CONTENT	vii – ix
	LIST OF TABLES	x
	LIST OF FIGURES	xi – xiii
	LIST OF ABBREVIATION	xiv
	LIST OF SYMBOLS	xv – xvii
1	INTRODUCTION	1 – 5
	1.1 Background	1 – 3
	1.2 Problem Statement	4
	1.3 Objectives	5
	1.4 Scope of Project	5
2	LITERATURE REVIEW	6 – 27
	2.1 Thermoacoustic	6 – 11
	2.1.1 General Formula	10 – 11
	2.2 Thermoacoustic Refrigerator	11 – 22
	2.2.1 Design of the Thermoacoustic Refrigerator	13 – 18
	2.2.2 Design of Stack	18 – 22
	2.3 CubePro 3D Printer	23 – 25
	2.4 Computational Fluid Dynamics (CFD) Simulation	25 – 27

3	METHODOLOGY	28 – 65
3.1	Flow Chart	28 – 31
3.2	Thermoacoustic Refrigerator Apparatus	32 – 43
3.2.1	Thermoacoustic Refrigerator Components	34
3.2.1.1	Loudspeaker Box	34
3.2.1.2	Resonator	35
3.2.1.3	Loudspeaker	36
3.2.1.4	Stack	36 – 39
3.2.1.5	Cover	39 – 40
3.2.1.6	Amplifier	40 – 41
3.2.1.7	Function Generator	42 – 43
3.2.2	Fabrication and Assembling	44 – 49
3.2.2	Fabrication and Assembling	44 – 45
3.2.3	Calibration and Debugging	45 – 46
3.2.4	Summary of Thermoacoustic Refrigerator	47 – 49
3.3	Computational Fluid Dynamics (CFD) Simulation	50 - 65
3.3.1	Geometry Drawing	50 – 52
3.3.2	Meshing	52 – 55
3.3.3	Mesh Checking	56 – 57
3.3.4	Solver Setting	58 – 63
3.3.5	Grid Independence Test Method	64
3.3.6	Validation Method	65
4	RESULT ANALYSIS AND DISCUSSION	66 – 80
4.1	Experimental Result	66 – 69
4.1.1	Experimental Result for 3D-Printed ABS Stack	66 – 67
4.1.2	Experimental Result for Stainless-Steel Scrubber Stack	68 – 69
4.2	Computational Fluid Dynamics (CFD) Results	69 – 78
4.2.1	Grid Independence Test	70
4.2.2	Model Validation	71 – 72

4.2.3	Pressure Result	72 – 74
4.2.4	Temperature Result	75 – 76
4.2.5	Velocity Result	77 – 78
4.3	Discussion	79 – 80
5	CONCLUSION AND RECOMMENDATION	81 – 84
5.1	Conclusion	81 – 82
5.2	Recommendation	83 – 84
	REFERENCES	85 – 92
	LIST OF APPENDICES	93 – 95
	APPENDIX A1 Drawing of ABS Stack	93
	APPENDIX A2 Gantt Chart for PSM 1	94
	APPENDIX A3 Gantt Chart for PSM 2	95



LIST OF TABLES

TABLE	TITLE	PAGE
2.1	Dimensionless parameters in the thermoacoustic refrigerator system	14
2.2	Materials' Thermal Properties Comparison	21
2.3	Nomenclature of Navier-Stokes Equations' Parameters	27
3.1	Action taken at Phase 1 (PSM 1)	29
3.2	Action taken at Phase 2 (PSM 2)	30
3.3	Specification of Flepcher FLP-MT1201 Amplifier	41
3.4	Specification of MCP SG1005 Function Generator	42 – 43
3.5	Thermoacoustic Refrigerator's Parameter (3D-Printed ABS Stack) Summary	48
3.6	Thermoacoustic Refrigerator's Parameter (Stainless-Steel Scrubber Stack) Summary	49
3.7	Details on Edge Meshing in ANSYS Meshing	53
3.8	Details on "MultiZone Quad/Tri" Inserted Mesh Method	54
3.9	Skewness and Aspect Ratio of Mesh Model	57
4.1	Percentage error of amplitude	72
4.2	Average temperature at both end points of ABS stack	76
4.3	Summary of Simulation Cases	79

LIST OF FIGURES

FIGURE	TITLE	PAGE
1.1(a)	Alpha Type Stirling Engine	2
1.1(b)	Beta Type Stirling Engine	2
1.2	Schematic Diagram of Thermoacoustic Refrigerator	3
2.1(a)	Schematic Diagram of a Thermoacoustic Refrigerator	7
2.1(b)	Schematic Diagram of a Thermoacoustic Engine	7
2.2	Thermoacoustic Stirling Engine	8
2.3	Schematic Diagram of Thermoacoustic Cycle	9
2.4	Thermoacoustic Refrigerator	12
2.5	Tabletop Thermoacoustic Refrigerator Apparatus	15
2.6	Stack's Cross-section in Thermoacoustic System	18
2.7	Specific Heat and Thermal Conductivity of Materials	21
2.8	CubePro 3D Printer	23
2.9	Build Settings of CubePro Software	24
2.10	BCC Single Unit Cell for 1 Complete Lattice Structure Block	24
3.1	Flow Chart of Methodology	31
3.2	Schematic Diagram of Thermoacoustic Refrigerator Apparatus	32
3.3	Thermoacoustic Refrigerator Experiment Rig	33
3.4	The Speaker Box of Thermoacoustic Refrigerator	34
3.5	Resonator of Thermoacoustic Refrigerator	35
3.6	Sound Driver for Thermoacoustic Refrigerator	36
3.7	Cross-section of 3D Printed Stack	37
3.8(a)	3D-Printed Stack	38
3.8(b)	Stainless-Steel Scrubber Stack	38
3.9	Cover for Thermoacoustic Refrigerator Resonator	39

3.10	Flepcher FLP-MT1201	40
3.11	MCP SG1005 Function Generator	43
3.12	V-Tech Acetic Silicone	44
3.13(a)	M4 Screws	45
3.13(b)	M4 Bold Nuts	45
3.14	PicoLog Data Logger TC 08	46
3.15	SENTRY ST-730 Hot Wire	46
3.16	Type K Thermocouples	46
3.17	2D Geometry Drawing in ANSYS	50
3.18	Geometry Dimension Parameters	51
3.19	Meshing Methods Used in ANSYS Meshing	52
3.20	Zoom in View of Mesh Display At Stack's Zone	55
3.21	Defined Named Selection on Boundaries	55
3.22	Mesh Size	56
3.23	Mesh Quality	56
3.24	General Setting Setup	58
3.25(a)	Specific heat Polynomial Profile of Air	59
3.25(b)	Thermal Conductivity Polynomial Profile of Air	59
3.26	Power Law Viscosity Profile of Air	59
3.27	Mass Flux Code for User-Defined Function	60
3.28	Solution Methods Configuration	61
3.29	Surface Monitor Setting	62
3.30	Run Calculation Configuration	63
4.1	Graph of temperature at two end points of 3D-Printed ABS stack against time	67
4.2	Graph of temperature at two end points of stainless-steel scrubber stack against time	68
4.3	x -Velocity at point-52 for different mesh densities	70
4.4	Comparison of x -velocity at Point-52 between the theoretical and simulation results	71
4.5	Pressure contour result from CFD simulation	73

4.6	Graph of pressure against x direction	73
4.7	Graph of pressure against time step at point-52	74
4.8	Temperature contour result from CFD simulation	75
4.9	Graph of temperature against x direction	75
4.10	Velocity contour result from CFD simulation	77
4.11	Graph of velocity against x direction	78
4.12	Velocity against number of time steps at point-52	78



LIST OF ABBREVIATION

ABS	Acrylonitrile Butadiene Styrene
ANSYS	Analysis System
COP	Coefficient of Performance
CFD	Computational Fluid Dynamics
FYP	Final Year Project
GA	Genetic Algorithm
MOGA	Multi-Objective Genetic Algorithm
Ph. D.	Doctor of Philosophy
PISO	Pressure-Implicit with Splitting of Operators
PLA	Polylactic Acid
PSM	Projek Sarjana Muda
SOGA	Single-Objective Genetic Algorithm
STL	Stereolithography
TA	Thermoacoustic
3D	Three Dimensions
UTeM	Universiti Teknikal Malaysia Melaka

LIST OF SYMBOLS

λ	=	Wavelength of sound
α	=	Speed of sound
f	=	Oscillation frequency
ρ	=	Density of air
k	=	Thermal conductivity
ω	=	Angular frequency
π	=	Pi (Mathematical constant for circle)
C_p	=	Specific heat per unit mass
κ	=	Diffusivity of gas
μ	=	Dynamic viscosity
ν	=	Kinematic viscosity
σ	=	Prandtl number
δ_y	=	Viscous penetration depth
δ_k	=	Thermal penetration depth
Q_c	=	Cooling Power
W	=	Acoustic Power
Q_{cn}	=	Normalized cooling power
W	=	Normalized acoustic power
δ_{kn}	=	Normalized thermal penetration depth
COP	=	Coefficient of performance
L_s	=	Stack length
L_{sn}	=	Normalized stack length
p_o	=	Dynamic pressure
p_m	=	Mean pressure
x_n	=	Normalized stack position

x_s	=	Stack center position
γ	=	Ratio of specific heat (Gamma)
y_o	=	Half spacing of the stack
J	=	Acoustic wave number
T_m	=	Mean Temperature
ΔT_m	=	Temperature difference across the stack
ΔT_{mn}	=	Normalized temperature difference
B	=	Blockage ratio (Porosity)
ΔT_{crit}	=	Critical longitudinal temperature gradient
η	=	Thermal efficiency
T_c	=	Cold end temperature
T_h	=	Hot end temperature
Q	=	Conservative variable sector
t	=	Time
E	=	Inviscid flux vector along the x-axis
x	=	Horizontal Cartesian coordinate
F	=	Inviscid flux vector along y-axis
y	=	Vertical Cartesian coordinate
E_v	=	Viscous flux vector along the x-axis
F_v	=	Viscous flux vector along the y-axis
e	=	Total energy per unit mass
T	=	Temperature
τ	=	Stress tensor
τ_{xx}	=	Stress tensor along x-axis
τ_{yy}	=	Stress tensor along y-axis
τ_{xy}	=	Stress tensor along xy-axis
v	=	Vertical velocity component
u	=	Horizontal velocity component
g	=	Gravitational acceleration, 9.81 m s^{-2}
P_l	=	Inlet oscillating pressure

m_I = Inlet mass flux
 θ = Phase difference



CHAPTER 1

INTRODUCTION

1.1 Background

Thermoacoustic (TA) system is a system that is able to produce either heating effect or cooling effect based on thermoacoustic principle. Thermoacoustic principles allow gas particles to expand, compress and exchange heat with adjacent surfaces to complete a thermodynamic cycle so that heating or cooling effect can be produced.

These processes take place inside a resonator without the use of any moving mechanism, except for the acoustic driver. Hence, it is greener technology than the conventional refrigerator or engine.

The meaning of “Thermoacoustic” (TA) is a field from combination of thermodynamic and acoustic fields which is self-explanatorily defined by Nikolaus Rott in 1980 (Rott, 1980). According to Swift (2001), the early stage of thermoacoustic was begun with Stirling engines since a century ago and the early concept of the Stirling engine was to produce work with the combination of crankshaft, piston, connecting rods, displacer, and et cetera while the structure of a Stirling engine is shown in Figure 1.1(a) and Figure 1.1(b) as in below.

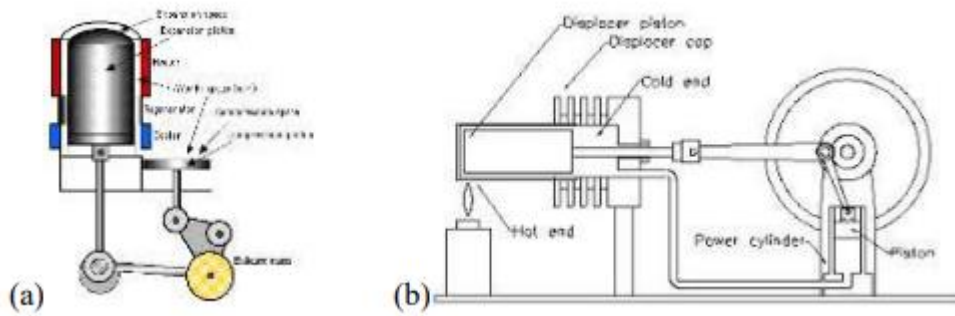


Figure 1.1: (a)Alpha Type Stirling Engine

(Retrieved from: <https://www.ohio.edu/mechanical/stirling/engines/engines.html>) and (b)Beta Type Stirling Engine

(Retrieved from: <https://www.webcomsknkwrks.com/schmstirl.jpg>)

Based on the analysis that was done in nineteenth century ago, powerful computational tools during that time had been used to analyze the four discrete steps of Stirling cycle, that is compression, displacement to and fro (two steps), and expansion in order to study the relation between the pressure change and velocity in the Stirling engine.

The studied analysis was based on extreme approximation in order to simplify the analysis or in another word, the analyzed Stirling cycle could be said as idealized cycle. Figure 1.2 below shows schematic diagram of how does a thermoacoustic engine work.

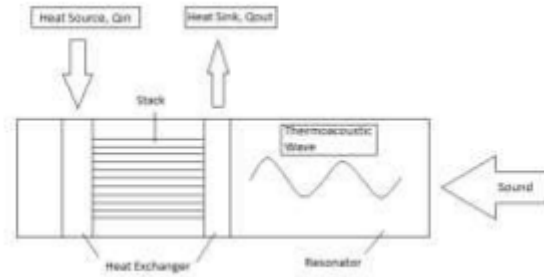


Figure 1.2: Schematic Diagram of Thermoacoustic Refrigerator

However, the study of Stirling cycle gave a sparking idea to Peter Ceperly that the phasing between pressure and velocity in the thermodynamic elements of Stirling machine is the same as the phasing between pressure and velocity in a traveling acoustic wave. As long as there is a phasing between pressure and velocity, there will be a temperature change and this concept leads to invention of thermoacoustic engine where the engine is used as heat exchanger or sub-cooler in both heat engine and refrigerator.

The components of a simple thermoacoustic engine is basically built from resonator, stack, and sound source. The two ends of the stack in the engine experience temperature increase and temperature decrease when a sound wave is passing through the stack. Due to this phenomenon, the thermoacoustic engine can be used as heat exchanger or sub-cooler in both heat engine and refrigerator.

1.2 Problem Statement

If the thermoacoustic engine is used as a heat exchanger or sub-cooler in power plant industry, the heat exchanger structure is much simpler than the commercial heat exchanger in power plant system and of course the cost is relatively cheaper than commercial heat exchanger. However, the work generated due to temperature change in thermoacoustic engine may be insufficient for huge electric energy generation. In order to obtain a higher efficiency or a more stable thermoacoustic system, the study of flow characteristic and heat transfer performance of the acoustic wave inside the thermoacoustic engine is very important to help us to understand the behavior of the acoustic wave.

Thermoacoustic has been studied by many researchers around the world but there are very few thermoacoustic laboratories available in Malaysia. Building a big and complicated thermoacoustic system may be costly especially for beginners. However, few researchers such as Zolpakar et al. (2017), Yap and Cruz (2015), and Russell and Weibull (2002) reputed on research activities on the thermoacoustic system just by building a small simple thermoacoustic engine or thermoacoustic refrigerator. Understanding thermoacoustic system is difficult without the help of working apparatus. Hence, there is a need to conduct feasibility study for a laboratory scale thermoacoustic apparatus. Moreover, most earliest experimental investigations of thermoacoustic system were not accompanied by appropriate Computational Fluid Dynamics (CFD) simulations. This makes it difficult to understand the fluid dynamics and thermodynamics properties of the system. Hence, a simple CFD model of the laboratory scale thermoacoustic system is also needed.

1.3 Objectives

The objectives of this study or project are:

- i. To design a small scale thermoacoustic prototype for experimentation.
- ii. To test the small scale thermoacoustic system using suitable measurement method.
- iii. To model a simple thermoacoustic flow field by using Computational Fluid Dynamics (CFD) software.

1.4 Scope of Project

This project is carried out experimentally and numerically. A simple thermoacoustic prototype will be developed using available cheap materials. A simple Computational Fluid Dynamics (CFD) model is also built by using ANSYS Fluent to provide additional details of flow behavior inside the system. This project is not covering details such as efficiency or stability of thermoacoustic engine, the fitness value and so on. This study is mainly focused on the study of flow of a thermoacoustic system. Therefore, the study concerns only the temperature at both ends of stack, pressure and velocity in thermoacoustic refrigeration system. Since this study is only focused on the resonator part of thermoacoustic system, either thermoacoustic refrigerator or thermoacoustic engine can be selected to be studied and hence, flow inside of thermoacoustic refrigerator system is chosen to be studied in this project.

CHAPTER 2

LITERATURE REVIEW

2.1 Thermoacoustic

Thermoacoustic is a study that focuses on the interaction between thermodynamic and acoustic which are about the energy conversion from sound kinetic to heat (thermoacoustic refrigerator) or heat to sound kinetic (thermoacoustic engine) (Ibrahim et al., 2011). Figure 2.1 (a) and Figure 2.1 (b) show schematic diagram of thermoacoustic refrigerator and schematic diagram of thermoacoustic engine respectively. Both are the same device but with two uses, depending on the source of energy given. Of course, based on the concept, thermoacoustic engine can be coupled with thermoacoustic refrigerator in replacement of sound generator in order to form complex single standing wave system (Desai et al., 2017).

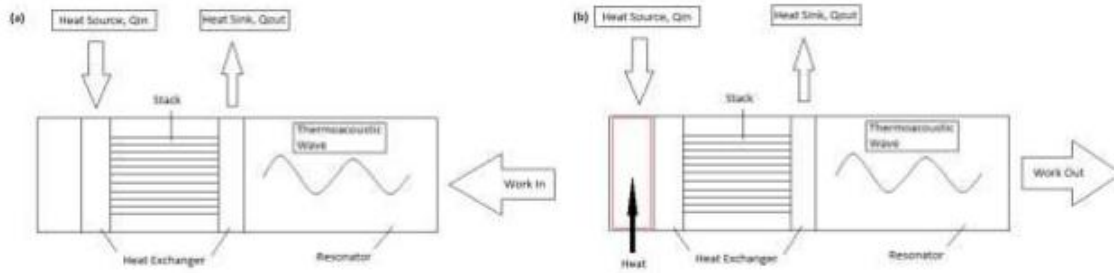


Figure 2.1: Schematic Diagram of a (a) Thermoacoustic Refrigerator and (b) Thermoacoustic Engine

Thermoacoustic devices can be divided into two types; standing wave devices and travelling wave devices. The difference between these devices is the phase difference between pressure and velocity. In standing wave, pressure is normally 90° out of phase with velocity while in travelling wave system, pressure and velocity are in phase.

Thermoacoustic engine generates work based on the acoustic wave principles driven by the air molecules through a heat source. According to Ferris (2018), as the heat applies on the end of stack, the air molecules will be vibrated and moved from hot end to cold end causing the expansion space to expand because the hot end pressure is high while the cold end pressure is low. Then, the pressure waves of heat and cold begin to vibrate back and forth between the stack making the chaotic wave fall into a steady rhythm. Chaotic waves with steady rhythm are also known as standing waves. Standing waves drive the piston in thermoacoustic engine to move back and forth and due to temperature difference, thermoacoustic engine able to perform work (Ferris, 2018).

Thermoacoustic engine device can convert heat into sound energy and vice versa (Napolitano et al., 2017). According to Napolitano et al. (2017), the wave theory of thermoacoustic engines can be categorized into standing wave which pressure and velocity of gas inside resonator is 90° in phase difference and travelling wave which pressure and velocity of gas are in phase. Another difference between standing wave and travelling wave is that standing wave is usually generated by a simple insulated resonator with stack and sound driver while travelling wave is usually generated through Stirling engine with mechanical pistons which is more complicated than standing wave in term of apparatus (Napolitano et al., 2017). Figure 2.2 shows a thermoacoustic Stirling engine.



Figure 2.2: Thermoacoustic Stirling Engine

(Retrieved from: <https://www.gyroscope.com/d.asp?product=ACOUSTIC>)

Thermoacoustic refrigerator produces work based on the standing wave principles driven by the air molecules but through a sound source. The standing wave in thermoacoustic refrigerator is as same as Stirling cycle which is depending on the pressure oscillation phase and out of phase with velocity oscillation phase. As sound source passes through the porous stack in resonator, air molecules in the standing wave is accelerated and cause the temperature change at both ends of the stack.

The concept is also based on the thermodynamic principles, that is fluid is expanded to cause temperature decrease and fluid is compressed to cause temperature increases; when two substances are placed together with direct contact, higher gradient heat will flow to lower gradient heat (Newman et al., 2016).

The process of thermoacoustic cycle consists of 4 steps which are expansion of sound wave, rejecting heat to stack, compression of sound wave, and absorption of heat from stack (Yap & Cruz, 2015). Figure 2.3 shows schematic diagram of a thermoacoustic cycle.

According to Yap and Cruz (2015), from process 1 to process 2, gas inside the thermoacoustic refrigerator is pressurized through compression and this will heat up the gas parcel as pressure drops (thermodynamics principle) causing the gas moves toward the hot side of the stack.

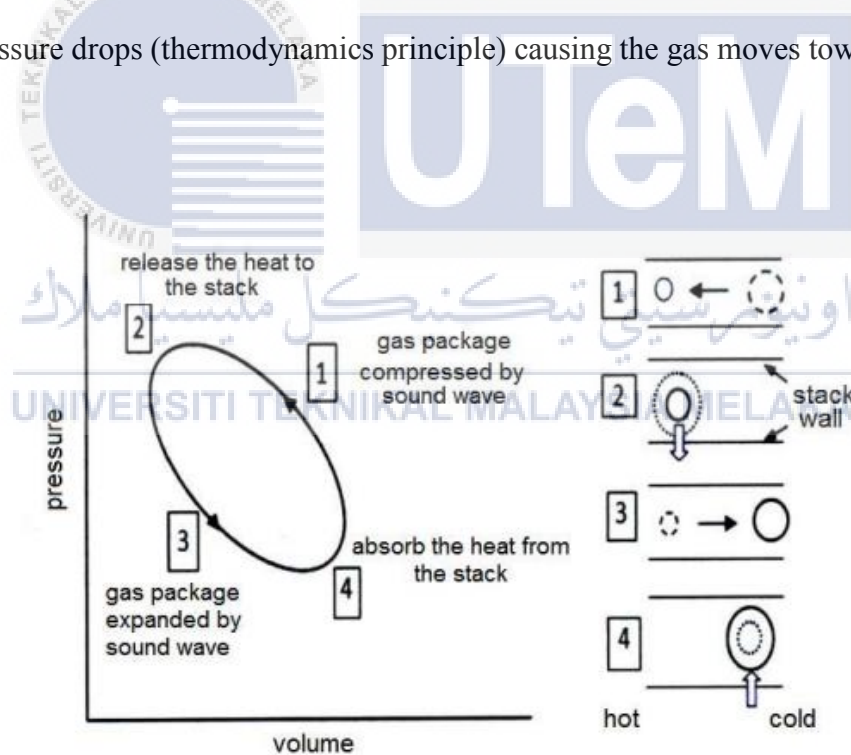


Figure 2.3: Schematic Diagram of Thermoacoustic Cycle (Dyatmika et al., 2015)

Referring to Figure 2.3, from process 2 to process 3, the heated gas which is hotter than the stack is then transferred to the stack walls and in this phase, pressure and displacement of gas are in phase (Yap & Cruz, 2015).

After that, during process 3 to process 4, gas parcel is then adiabatically depressurized by expansion, this decreases the temperature of the gas parcel due to pressure drop (thermodynamic principle) and displaces the gas towards the cold side (Yap & Cruz, 2015).

Lastly, the gas parcel undergoes isobaric process again by absorbing heat from the system environment and the cycle repeats again (Yap & Cruz, 2015).



2.1.1 General Formula

In order to investigate the flow inside a thermoacoustic system, one must understand the formulas and terminologies in thermoacoustic field. Generally, there are few terminologies and formulas that are important in thermoacoustic system such as wavelength of sound, λ in Eq. (2.1), thermal penetration depth, δ_k in Eq. (2.2), viscous penetration depth, δ_v in Eq. (2.3), and gas displacement amplitudes, ξ_l (Swift, 2001).

$$\lambda = a / f \quad (2.1)$$

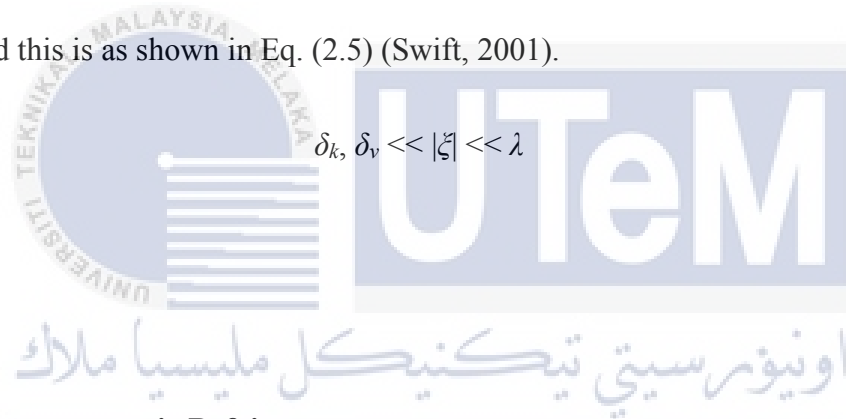
$$\delta_k = \sqrt{2k / \omega \rho C_p} = \sqrt{2\kappa / \omega} \quad (2.2)$$

$$\delta_v = \sqrt{2\mu / \omega \rho} = \sqrt{2\nu / \omega} \quad (2.3)$$

where a is speed of sound, f is oscillation of frequency, k is thermal conductivity, ω is angular frequency which is equivalent to $2\pi f$, ρ is density of gas, C_p is specific heat per unit mass at constant pressure, κ is diffusivity of the gas, μ is gas dynamic viscosity, and ν is gas kinematic viscosity (Swift, 2001). The square of the viscous penetration depth divided by thermal penetration depth is equivalent to Prandtl number, σ as shown in Eq. (2.4).

$$\left(\frac{\delta_v}{\delta_k}\right)^2 = \frac{\mu C_p}{k} = \sigma \leq 1 \quad (2.4)$$

However, in a common acoustic, there is a limitation between the gas displacement amplitudes with viscous penetration depth or thermal penetration depth and the wavelength of the sound and this is as shown in Eq. (2.5) (Swift, 2001).



$$\delta_k, \delta_v \ll |\xi| \ll \lambda \quad (2.5)$$

2.2 Thermoacoustic Refrigerator

Thermoacoustic refrigerator system is an alternative environmentally friendly cooling system which is firstly invented by Hofler in 1986 (Hofler, 1989). Figure 2.4 shows a drawing of a thermoacoustic refrigerator which uses standing wave.

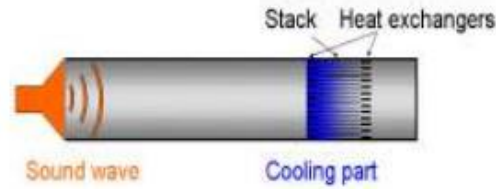


Figure 2.4: Thermoacoustic Refrigerator

(Retrieved from: <http://talk4technology.blogspot.com/2016/07/thermo-acoustic-refrigeration.html>)

Although the thermoacoustic refrigerator has been proven to operate well but it is still inconvenient to be installed as a commercial refrigerator because the size of thermoacoustic Stirling refrigerator is big (Chin, 2017). According to Chin (2017), thermoacoustic refrigerator had been developed to be applied to launch on the Space Shuttle Discovery in January 1992 and there was no heat supplied to the cooler system. Thus, the size was big in order to achieve large temperature difference for about 118 K.



The first study of coaxial thermoacoustic refrigerator was started by Poese et al. (2004) in cooperation between Pennsylvania State University and Ben & Jerrys Company to develop an economical friendly ice cream freezer. The gas used in the thermoacoustic refrigerator was helium in which the working fluid at under pressure of 1 MPa and it was driven by moving magnetic motor at 100 Hz of frequency (Poese et al., 2004).

2.2.1 Design of Thermoacoustic Refrigerator

A Doctor of Philosophy (Ph. D.) research had been done by Tijani et al. (2001) regarding the loudspeaker-driven thermoacoustic refrigerator by researching articles, journals, and other sources. The governing equations of thermoacoustic refrigerator is introduced by Tijani et al. (2001) and simplified to be used in thermoacoustic refrigerator. According to Tijani et al. (2002), the coefficient of performance (*COP*) of a thermoacoustic refrigerator system is given by Eq. (2.6), where normalized cooling power, Q_{cn} and normalized acoustic power, W_n are described in Eq. (2.7) and Eq. (2.8) respectively. Table 2.1 shows the details of symbols used in Eq. (2.7) and Eq. (2.8).

$$COP = \frac{Q_{cn}}{W_n} \quad (2.6)$$

$$Q_{cn} = \frac{\delta kn D^2 \sin 2xn}{8\gamma(1+\sigma)A} \cdot \left[\frac{\Delta T m n \tan xn}{(\gamma-1)B L s n} \cdot \frac{1+\sqrt{\sigma}+\sigma}{1+\sqrt{\sigma}} - (1 + \sqrt{\sigma} - \sqrt{\sigma} \delta kn) \right] \quad (2.7)$$

$$W_n = \frac{\delta kn L s n D^2}{4\gamma} (\gamma-1) B \cos^2 xn \cdot \left(\frac{\Delta T m \tan xn}{B L s n (\gamma-1)(1+\sqrt{\sigma})A} \right) - \frac{\delta kn L s n D^2}{4\gamma} \cdot \frac{\sqrt{\sigma} \sin^2 xn}{BA} \quad (2.8)$$

where A from Eq. (2.8) can be defined as in Eq. (2.9) as shown as in below:

$$A = 1 - \sqrt{\sigma} \delta kn + 0.5 \sigma \delta kn \quad (2.9)$$

From Eq. (2.6), (2.7), (2.8), (2.9) and Table 2.1, x is the distance from driver surface, Q_c is cooling power, W is acoustic power, p_o is dynamic pressure, p_m is mean pressure, a is speed of sound, T_m is mean temperature, ΔT_m is temperature difference across the stack, L_s is the stack length, γ (gamma) is specific heat ratio, y_o is half spacing of the stack, δ_k is thermal penetration depth, and J is acoustic wave number.

Table 2.1: Dimensionless parameters in the thermoacoustic refrigerator system

(Tijani et al., 2002)

Operation parameters	
Drive ratio:	$D = p_o / p_m$
Normalized cooling power:	$Q_{cn} = Q_c / p_m a A$
Normalized acoustic power:	$W_n = W / p_m a A$
Normalized temperature difference:	$\Delta T_{mn} = \Delta T_m / T_m$
Gas parameters	
Ratio of specific heat:	γ (gamma)
Prandtl number:	σ
Normalized thermal penetration depth:	$\delta_{kn} = \delta_k / y_o$
Stack geometry parameters	
Wave number:	$J = 2\pi / \lambda$
Normalized stack length:	$L_{sn} = JL_s$
Normalized stack position:	$x_n = Jx$
Blockage ratio or porosity:	$B = y_o / (y_o + l)$

A tabletop apparatus was set up by Russel and Weibull (2002) and the tabletop model is shown in Figure 2.5. To make a thermoacoustic refrigerator work, the gas, stack, rsonator, stack's position is very crucial (Yap & Cruz, 2015).

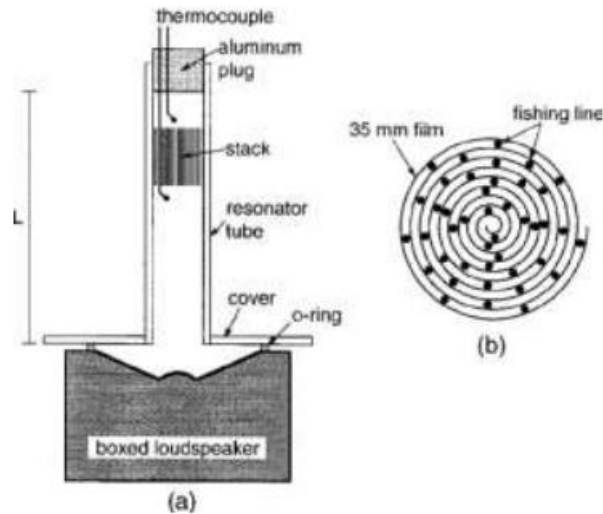


Figure 2.5: Tabletop Thermoacoustic Refrigerator Apparatus

(Retrieved from: https://www.researchgate.net/figure/a-Schematic-diagram-of-the-demonstration-thermoacoustic-refrigerator-b-cross_fig1_243492353)

According to Russel and Weibull (2002), the tabletop model of thermoacoustic refrigerator is built just for demonstration in order to make a beginner to understand the thermoacoustic concept. The model is built by winding 35 mm photographic film as stack, placing acrylic tube on a loudspeaker as a resonator and sealed with o-ring, closing the end of acrylic tube with aluminium plug, and inserting thermocouple into both ends of stack to take the temperature reading. The critical longitudinal temperature gradient is related to acoustic pressure, p , displacement amplitude, ξ , density, ρ , and specific heat, C_p of air molecules while the equation is expressed in Eq. (2.10) (Swift, 2001).

$$\Delta T_{crit} = \frac{p}{\xi \rho C_p} \quad (2.10)$$

According to Dhuley and Atrey (2010), there are assumptions made by them in the design guideline for thermoacoustic refrigerator before their thermoacoustic refrigerator is built. Firstly, short stack approximation which means the stack length is very small compared to the wavelength of the standing wave, $L_s \ll \lambda$ so that the pressure and velocity amplitudes of standing wave gas inside the resonator are assumed as equal or less than the stack length. Besides, the conductivity of the plate material is ignored and temperature across the stack ends is assumed to be smaller than the mean temperature. Then, the flow of gas that is helium is inviscid by neglecting the friction between gas molecules and inner wall of the resonator. Next, the experiment is occurred in steady state of refrigerator operation, that is the mean temperature and temperature across the stack ends are constant after the offset time (Dhuley & Atrey, 2010).

Dhuley and Atrey (2010) use helium as their thermoacoustic refrigerator gas which travels in speed of 935 m s^{-1} , has thermal conductivity, $k = 0.14 \text{ W m}^{-1} \text{ K}^{-1}$, specific ratio, $\gamma = 1.67$, and the result of the experiment is recorded with cooling power of 2 W and cold end temperature of 210 K .

Yap and Cruz (2015) have done research of thermoacoustic refrigerator which records efficiency of 42.96% . They use Corning Celcor Ceramic with different length (in range of 3 cm to 4 cm), Pyrex test tube from Penn State as resonator, and air as wave medium. They use thermodynamic equation as shown in Eq. (2.11) for calculating the thermal efficiency instead of using equations from Tijani et al. (2002).

$$\eta = 1 - \frac{T_c}{T_h} \quad (2.11)$$

where η is thermal efficiency, T_c is cold end temperature, and T_h is hot end temperature.

Researches from Dhuley and Atrey (2010), Russel and Weibull (2002), and Yap and Cruz (2015) can be said as very good introduction, explanation and demonstration for a beginner to understand the thermoacoustic concepts in terms of theoretical and experimental. Therefore, their articles can be recommended only for understanding the thermoacoustic concepts but in order to increase the coefficient of performance, *COP* or efficiency of thermoacoustic refrigerator, additional findings such as methods and solutions for optimizing thermoacoustic system are needed.

Tijani et al. (2002) introduces the theory on how coefficient of performance of thermoacoustic refrigerator is affected by parameters as shown in Eq. (2.6), (2.7), (2.8) and (2.9). Zolpakar et al. (2014) implement the optimization of stack to increase the coefficient of performance by using multi-objective genetic algorithm (MOGA) and compares the result with the result from Tijani et al. (2002) (Zolpakar et al., 2014).

Later on, optimizing the thermoacoustic refrigerator has been done by using single objective genetic algorithm (SOGA) method which is believed able to achieve coefficient of performance, *COP* of 1.58 and 1.64 for helium and helium-xenon gas respectively (Zolpakar et al., 2016). Then, Zolpakar et al. (2016) have implemented an experiment to investigate the coefficient of performance of standing wave in thermoacoustic refrigerator by using multi-objective genetic algorithm (MOGA) (Zolpakar et al., 2016).

Zolpakar et al. (2016) successfully use the governing equations as shown in Eq, (2.6), (2.7), (2.8) and (2.9) from Tijani et al. (2002) in designing her thermoacoustic refrigerator and with the optimized stack that is done by using MOGA. Coefficient of performance is increased by 5.4%.

2.2.2 Design of Stack

Figure 2.6 shows a cross-section of thermoacoustic system stack. Referring to Figure 2.6, the design of stack in thermoacoustic system has relation with the thermal penetration depth and the blockage ratio (Bhavya, 2013). Thus, the design of stack can affect the normalized acoustic power, normalized cooling power, and the coefficient of performance, *COP* of the thermoacoustic refrigerator. There are two roles of stack in thermoacoustic system; as an accelerator to accelerate the air molecules to move back and forth and also as an insulator to keep the hot side to be insulated from the cold side (Ferris, 2018).

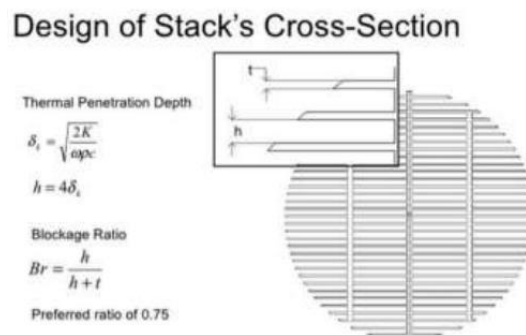


Figure 2.6: Stack's Cross-section in Thermoacoustic System
 (Retrieved from: https://www.slideshare.net/bhv_r/tar-20186393)

According to Zolpakar et al. (2017), a stack of thermoacoustic refrigerator is designed by using 3D-printer, Stratasys objet24 with the ink being polyjet photopolymer which the material used is VeroWhitePlus Rgd835 which has specific heat of $1 \text{ kJ kg}^{-1} \text{ K}^{-1}$ and thermal conductivity, $k = 0.23 \text{ W m}^{-1} \text{ K}^{-1}$ which is higher than Mylar material but lower than Celcor Ceramic material. The experiment used an acrylic resonator which has quarter-wavelength of 400 Hz resonance frequency and diameter of 34 mm (Zolpakar et al., 2017).

The power density can be increased if the stack length is increased because of more interactions between gas molecules and stack in resonator (Zolpakar et al., 2017). Although the power density is increased by increasing stack length, the pressure will drop as well. Therefore, the optimized stack length is studied by Zolpakar in her 3D-printed stack and the stack length parameters used in the research are 3.5 cm, 4 cm, and 4.5 cm (Zolpakar et al., 2017).

According to Tijani et al. (2002), the approximation of stack length is approximately four times smaller than the inverse of wave number in DeltaE simulation assumption. In DeltaE simulation assumption, the temperature difference across the stack, ΔT_m is also approximately four times smaller than the mean temperature, $T_m = 250 \text{ K}$. The frequency used in Tijani et al. (2002), f is at 409 Hz, the stack length, L_s is 8.5 cm, and mean temperature, p_m is 100 kPa. The result of cold end temperature, T_c is recorded at 229 K with cooling power, Q_c of 3.5 W.

From the single-objective genetic algorithm (SOGA) that is done by Zolpakar et al. (2016) to optimize the parameters of the stack, it is found that the normalized stack length, L_{sn} , normalized center position of stack, x_{sn} , blockage ratio, B and drive ratio, D must be in the range as stated below in order to allow the thermoacoustic refrigerator to work in optimum condition.

$$0 \leq L_{sn} \leq 1$$

$$0.06 \leq x_{sn} \leq 0.42$$

$$0.67 \leq B \leq 0.8$$

$$0.015 \leq D \leq 0.03$$

The parameters above are options for designing the stack in thermoacoustic refrigerator but however, the exact optimized value of parameters for maximum coefficient of performance (*COP*) are still needed to be found through genetic algorithm (GA) analysis.

In the GA analysis, the function that is used in the analysis is the function, $f(X) = COP(X)$ (Zolpakar et al., 2016). The operation parameters used in the analysis are mean pressure, $p_m = 100$ kPa, mean temperature, $T_m = 250$ K, normalized temperature difference, $\Delta T_{mn} = 0.3$, drive ratio, $D = 0.02$, and oscillating frequency of 400 Hz. Helium gas is selected with speed in helium gas, $a = 935$ m s⁻¹. Prandtl number, $\sigma = 0.68$, specific heat ratio, $\gamma = 1.67$, blockage ratio, $B = 0.75$, acoustic wave number, $J = 0.373$ m⁻¹ and normalized thermal penetration depth, $\delta_{kn} = 0.66$.

As the result of the analysis, the optimized parameters obtained are stack center position, $x_s = 3.57$, stack length, $L_s = 3$ cm, blockage ratio, $B = 0.8$ and drive ratio, $D = 0.026$ and the *COP* is 26% higher than the *COP* that is found by Tijani et al. (2002).

However, Desai et al. (2017) has tried a different way for finding the optimized parameters but using response surface methodology (RSM) with association of DeltaEC software for simulation. The finding objective of Desai et al. (2017) is the same as Zolpakar et al. (2016) but in different method.

As stated by Zolpakar et al. (2016), the stack needs to have a spacing in between two thermal penetration depth to four thermal penetration depth that is $2\delta_k \leq 2y_o \leq 4\delta_k$. Figure 2.7 and Table 2.2 show the specific heat and thermal conductivity properties for different materials such as Celcor, Reticulated Vitreous Carbon (RVC) and Mylar and the comparison of materials' thermal properties such as Acrylonitrile Butadiene Styrene (ABS), Celcor, Reticulated Vitreous Carbon (RVC) and Mylar (Zolpakar et al., 2016)..

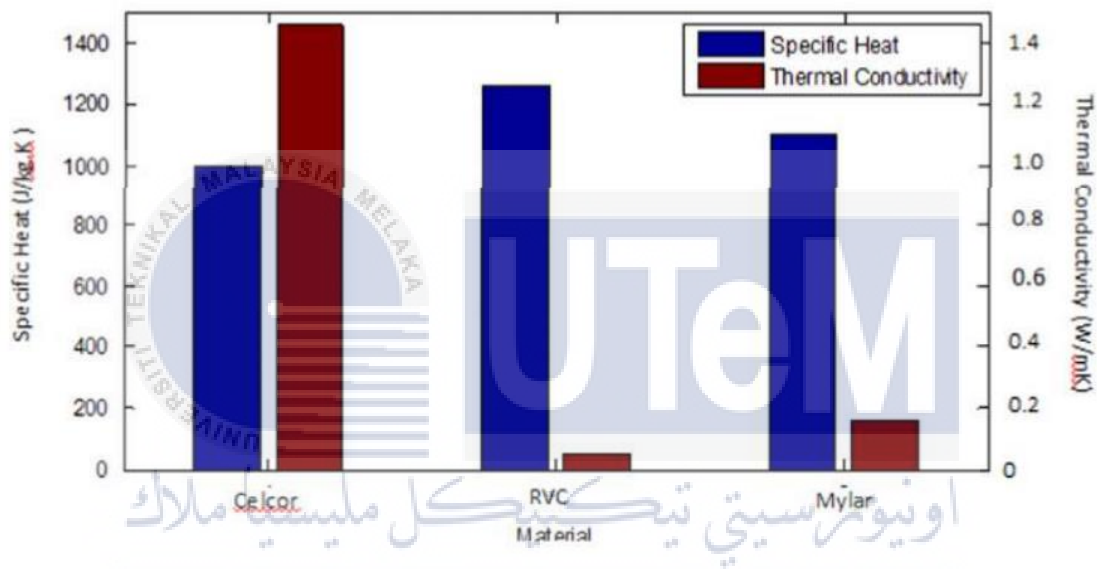


Figure 2.7: Specific Heat and Thermal Conductivity of Materials (Zolpakar et al., 2016)

Table 2.2: Materials' Thermal Properties Comparison (Zolpakar et al., 2016)

Thermal Properties Comparison		
Materials	Specific Heat, C_p ($J\ kg^{-1}\ K^{-1}$)	Thermal Conductivity, k ($W\ m^{-1}\ K^{-1}$)
Celcor	1000	1.5
RVC	1260	0.033 – 0.05
Mylar	1100	0.2

From Figure 2.7, it is shown that RVC has the highest specific heat, C_p up to 1200 $\text{J kg}^{-1}\text{K}^{-1}$ and the lowest thermal conductivity, k up to $0.05 \text{ W m}^{-1} \text{ K}^{-1}$, Celcor has the lowest specific heat, $C_p = 1000 \text{ W kg}^{-1}\text{K}^{-1}$ and the highest thermal conductivity, $k = 1400 \text{ W m}^{-1} \text{ K}^{-1}$. Mylar material's properties are in between Celcor and RVC which has specific heat, C_p up to $1300 \text{ W kg}^{-1} \text{ K}^{-1}$ and thermal conductivity, k up to $0.2 \text{ W m}^{-1} \text{ K}^{-1}$ (Zolpakar et al., 2016). Acrylonitrile Butadiene Styrene (ABS) material has thermal conductivity, k of $0.195 \text{ W m}^{-1} \text{ K}^{-1}$ and specific heat, C_p of $1420 \text{ J kg}^{-1} \text{ K}^{-1}$.



2.3 CubePro 3-Dimensional Printer

CubePro 3-Dimensional (3D) printer can be used in home for building 3 dimensions Acrylonitrile Butadiene Styrene (ABS) or Polylactic Acid (PLA) object with the association of computer software (3D Systems, 2017). Figure 2.8 shows a CubePro 3D printer.



Figure 2.8: CubePro 3D Printer

(Retrieved from: <https://www.3dsystems.com/shop/support/cubepro/faq>)

A Computer Aided Drawing (CAD) must be saved in stereolithography (STL) format so that the CubePro computer software application is able to read the drawing. Then, the drawing is needed to be built and it is required to undergo slicing so that it can be saved into cubepro format file to begin the 3D printing process. However, there are options in the build settings to be chosen in the printing process which can be categorized into layer resolution, print strength, and print pattern.

The layer resolution consists of three layer types such as 70 μm , 200 μm , and 300 μm . The print strength can be hollow, strong, almost solid and solid while the print pattern can be cross, diamonds and honeycomb. Figure 2.9 shows the build settings in CubePro software.

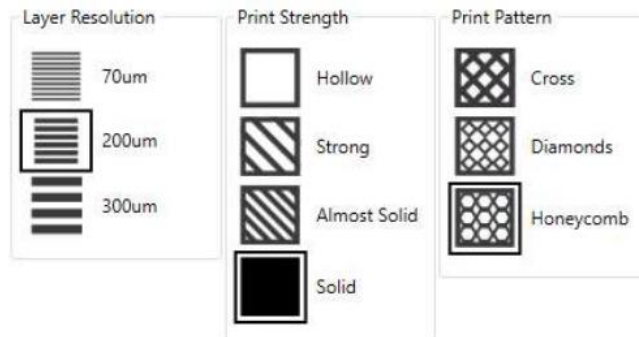


Figure 2.9: Build Settings of CubePro Software

The selection of the layer resolution print strength and print pattern is very important because it decides the strength of the printed product. Lattice structure is a periodic open cell structure like body-centred-cubic (BCC) for its microstructure as shown in Figure 2.10 (Rosli et al, 2017).



Figure 2.10: BCC Single Unit Cell for 1 Complete Lattice Structure Block

(Rosli et al., 2017)

According to Rosli et al. (2017), an experiment has been done to look for the stress-strain graph of different layer thickness and for variety layer thickness of 20 cm x 20 cm x 20 cm ABS cubes printed by CubePro 3D printer. It is found that the shorter the layer thickness, the greater the interlayer bonding but product printed by 200 µm layer thickness produces reasonable mechanical response because the strength of long flat plateau is good.

2.4 Computational Fluid Dynamics (CFD) Simulation

Computational Fluid Dynamics (CFD) simulation is common computer aided software to analyze the flow of most cases in this world. There are few researchers who use CFD simulation software to simulate the flow condition in order to study the behavior of the flow.

By using CFD simulation, researchers are able to save development cost, able to have quick assessment on study, able to clearly understand the information from CFD result, and able to simulate multiple conditions of flow (PRE Technologies Ltd, 2014).

According to Sharify et al. (2016) in his CFD simulation, the researchers described two-dimensional (2D) Navier- Stokes equation in the simulation as shown in Eq. (2.12) below to identify the flow as compressible and turbulence flow and the stress tensor components are defined in Eq. (2.13), (2.14), and (2.15).

$$\frac{\partial Q}{\partial t} + \frac{\partial E}{\partial x} + \frac{\partial F}{\partial y} = \frac{\partial Ev}{\partial x} + \frac{\partial F}{\partial y}, \text{ where} \quad (2.12)$$

$$Q = \begin{bmatrix} \rho \\ \rho\mu \\ \rho v \\ \rho e \end{bmatrix}, E = \begin{bmatrix} \rho v \\ \rho\mu^2 + p \\ \rho\mu v \\ (\rho e + p)\mu \end{bmatrix}, F = \begin{bmatrix} \rho\mu \\ \rho v\mu \\ \rho v^2 + p \\ (\rho e + p)v \end{bmatrix}, E_v = \begin{bmatrix} 0 \\ \tau_{xx} \\ \tau_{xy} \\ \tau_{xx}\mu + \tau_{xy}v + \kappa T_x \end{bmatrix}, \text{ and}$$

$$F_v = \begin{bmatrix} 0 \\ \tau_{yx} \\ \tau_{yy} \\ \tau_{yx}\mu + \tau_{yy}v + \kappa T_y \end{bmatrix}.$$

$$\tau_{xx} = \frac{2}{3} \mu (2u_x - v_y) \quad (2.13)$$

$$\tau_{yy} = \frac{2}{3} \mu (2v_y - u_x) \quad (2.14)$$

$$\tau_{yx} = \tau_{xy} = \mu (u_y - v_x) \quad (2.15)$$

The relation of pressure, p and total energy e per unit mass and the temperature in the energy equation are shown in Eq. (2.16) and Eq (2.17) in below while the relationship between the temperature and the others parameters are defined in Eq. (2.18), (2.19), and (2.20) (Sharify et al., 2016).

$$\rho e = \frac{p}{\gamma-1} + \frac{1}{2} \rho (u^2 + v^2) \quad (2.16)$$

$$C_p T = e + \frac{p}{\rho} - \frac{1}{2} (u^2 + v^2) \quad (2.17)$$

$$\alpha = (\kappa t - \kappa s) \kappa T = \left(\frac{1}{\gamma P} - \frac{1}{P} \right) \kappa T \quad (2.19)$$

$$\mu = \alpha \sigma \rho \quad (2.20)$$

where κ , κ_t , κ_s , α , P and σ are thermal conductance, isothermal compressibility, thermal diffusivity, reference pressure, and Prandtl number respectively. Table 2.3 shows the nomenclature of parameters used in Eq. (2.11), (2.12), (2.13), and (2.14).

Table 2.3: Nomenclature of Navier-Stokes Equations' Parameters (Sharify et al., 2016)

Parameters	Nomenclature
Q	Conservative variable sector
t	Time
E	Inviscid flux vector along the x -axis
x	Horizontal Cartesian coordinate (m)
F	Inviscid flux vector along y -axis
y	Vertical Cartesian coordinate (m)
E_v	Viscous flux vector along the x -axis
F_v	Viscous flux vector along the y -axis
ρ	Density (kg m^{-3})
μ	Dynamic viscosity (Pa s)
ν	Kinematic viscosity ($\text{m}^2 \text{s}^{-1}$)
e	Total energy per unit mass (J kg^{-1})
T	Temperature (K)
τ	Stress tensor (Pa)
v	Vertical velocity component (m s^{-1})
u	Horizontal velocity component (m s^{-1})

CHAPTER 3

METHODOLOGY

3.1 Flow Chart

In this subsection, the flow chart of this project is as shown in Figure 3.1 and is described with the help of Table 3.1 and Table 3.2 for Final Year Report part 1 (FYP 1) and FYP 2, respectively. To simplify the flow chart, the works for Projek Sarjana Muda (PSM) are separated into two, PSM 1 and PSM 2 in order to achieve the objective, the actions that need to be taken are listed in Table 3.1 and 3.2.

Figure 3.1 shows the flow chart of methodology of the flow of study for the thermoacoustic system. Literature review researching is being repeated throughout the whole Projek Sarjana Muda (PSM) 1 and 2. The brief explanation of literature review is not included in this section but it is described in Chapter 2 (Literature Review).

Table 3.1: Action taken at Phase 1 (PSM 1)

Action taken at phase 1 (PSM 1)		
No.	Action	Description
1.	Design of Stack.	Design the stack using SolidWorks software.
2.	Fabricate and 3D printing.	Purchase and fabricate the acrylic tube and box, at the same time 3D print the drawn stack by using 3D printer.
3.	Assembling and instrumentation setup.	Assemble the fabricated and 3D printed apparatus. Setup instrument for measurement.
4.	Collect data.	Implement experiment and collect data.
5.	Analysis.	Analyze experiment data.
6.	Documentation.	Technical report for PSM 1 is being written and summarized in order to be submitted.

Table 3.2: Action taken at Phase 2 (PSM 2)

No.	Action	Description
1.	Develop CFD model.	Draw the stack and its environment as model so that the model able to be simulated and analyzed.
2.	Mesh size.	Mesh the size of the model in CFD simulation.
3.	Set up boundary condition and solution for model solution.	Insert the boundary condition of model before progressing simulation.
4.	Constraint check.	Identify and check the constraint of the simulation.
5.	Grid independence check.	Identify and check the grid independence. If there is an error in grid independence, step 3 to step 6 are repeated.
6.	Analysis and discussion.	Analyze the Computer Fluid Dynamics (CFD) simulation result with small scale experiment result.
7.	Documentation.	Technical report for PSM 2 is being written and summarized in order to be submitted.

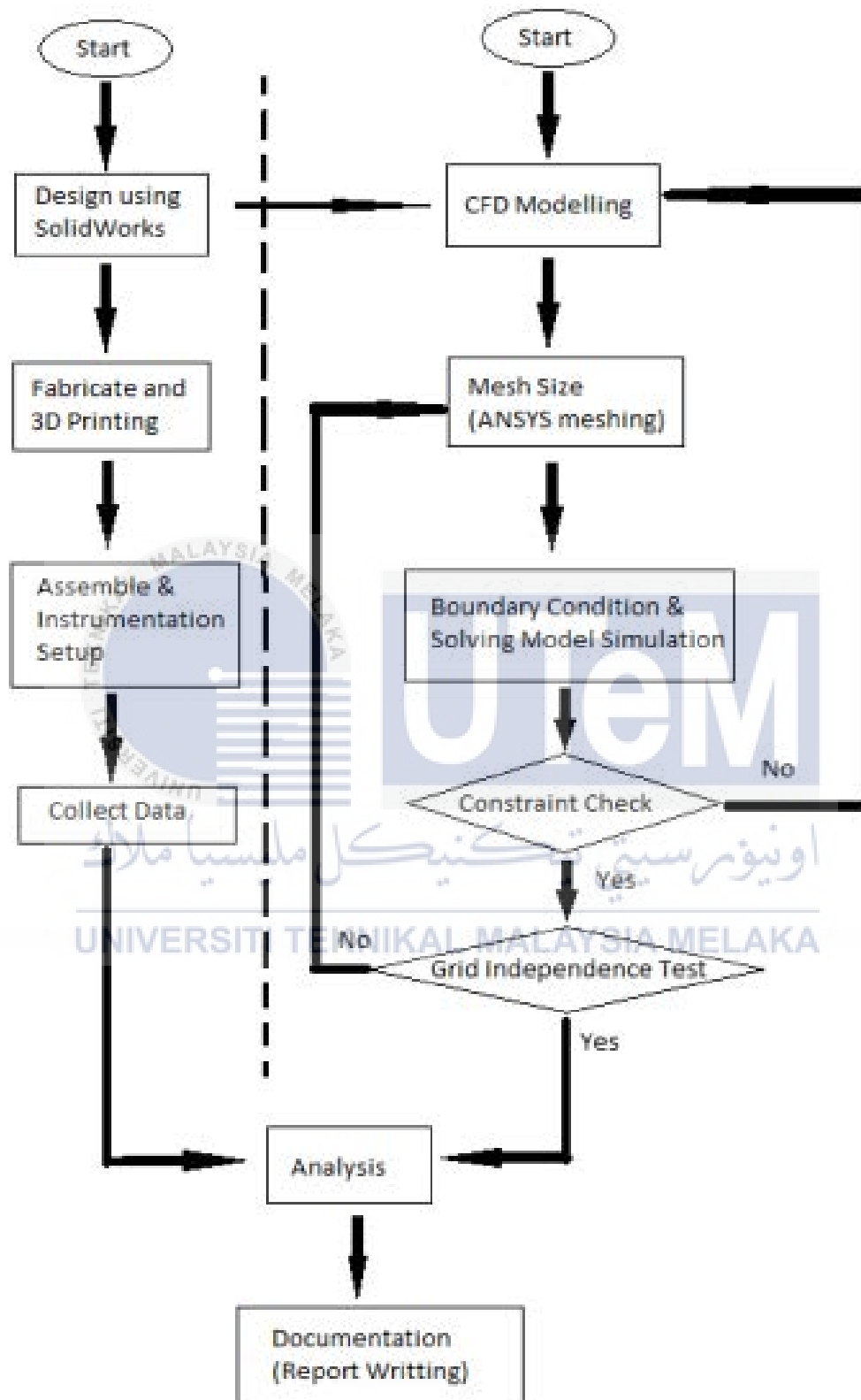


Figure 3.1: Flow Chart of Methodology

3.2 Thermoacoustic Refrigerator Apparatus

A thermoacoustic device like thermoacoustic refrigerator prototype is needed in order to implement an experiment to study the flow inside a thermoacoustic device. Figure 3.2 shows the schematic diagram of the thermoacoustic refrigerator prototype. It consists of a loudspeaker, a loudspeaker box, a resonator, a stack, a cover, a stand, an amplifier, a function generator, and a power source.

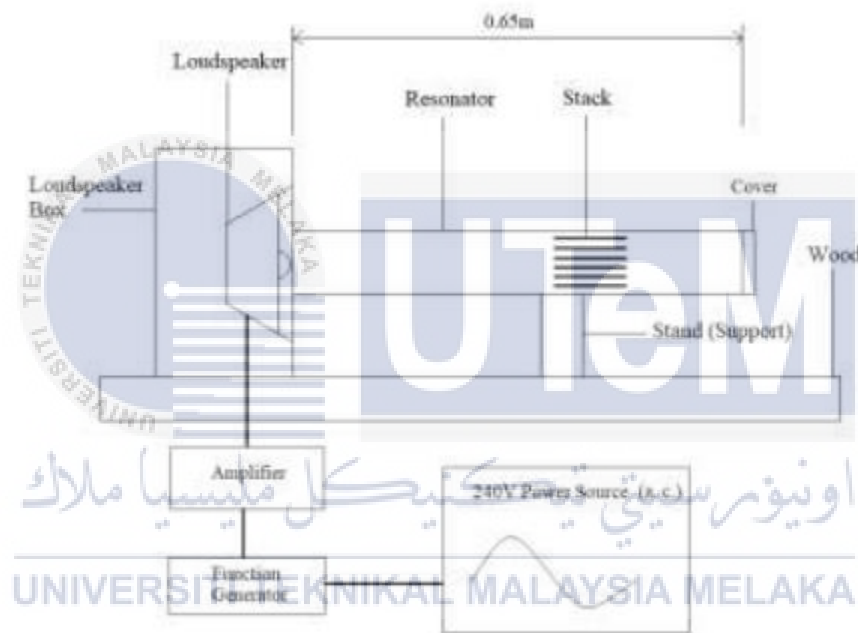


Figure 3.2: Schematic Diagram of Thermoacoustic Refrigerator Apparatus

Material and apparatus selection is very important in order to allow the thermoacoustic refrigerator to work. The power source is a sinusoidal alternative current with 240 V of voltage. A brief explanation will be explained in section 3.2.1 about the components of thermoacoustic refrigerator, including the resonator, stack, loudspeaker, amplifier and function generator.

The coming subsections will explain briefly on the selection of materials, specification of components such as loudspeaker, amplifier, function generator, acrylic box, acrylic tube, stack and so on. Figure 3.3 shows the thermoacoustic refrigerator experiment rig that is used in the laboratory.

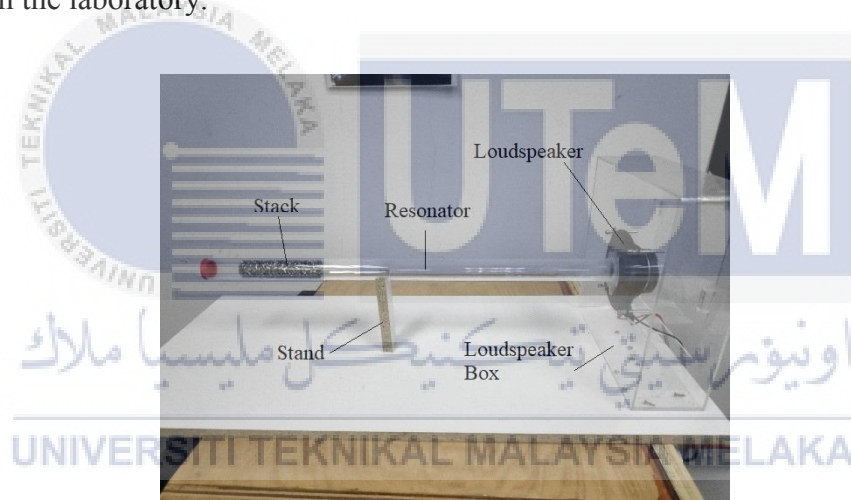


Figure 3.3: Thermoacoustic Refrigerator Experiment Rig

3.2.1 Thermoacoustic Components

3.2.1.1 Loudspeaker Box

Throughout the researches that have been studied by Zolpakar et al. (2017), Yap and Cruz (2015), Dhuley and Atrey (2010), and Russell and Weibull (2002), the most adaptable research to be referred to is Zolpakar et al. (2017) research because the surrounding temperature, materials used and operation parameters are reasonably within the Malaysia environment. All researches, however, give good introduction and overview for a beginner to understand the concept of thermoacoustic refrigerator. Dhuley and Atrey (2010) use of helium as their standing wave medium in their thermoacoustic refrigerator, but in this project, air is selected instead of helium because helium requires higher cost and better insulation compared to air.

The thermoacoustic refrigerator apparatus consists of resonator, sound driver, driver box, resonator, stack, function generator, and amplifier. The speaker box is made of 30cm x 30 cm x 10 cm customized acrylic box with a 3.1 cm center hole on top surface (30 cm x 30 cm) and 20 cm x 20 cm lockable door at the bottom surface (30 cm x 30 cm) is as shown in Figure 3.4.



Figure 3.4: The Speaker Box of Thermoacoustic Refrigerator

(Retrieved from: <https://thestationeryshop.com.sg/shop/display-and-presentation/display-and-presentation-acrylic-stand/acrylic-lucky-draw-box-cw-key/>)

3.2.1.2 Resonator

The resonator is made from acrylic tube with 3.5 cm outer diameter, 3.1cm inner diameter, and 0.65 m length is as shown in Figure 3.5. The acrylic material has thermal conductivity, k in range of $0.187 \text{ W m}^{-1} \text{ K}^{-1}$ to $0.209 \text{ W m}^{-1} \text{ K}^{-1}$ and specific heat, C_p in range of $1.46 \text{ J g}^{-1} \text{ }^\circ\text{C}^{-1}$ to $2.16 \text{ J g}^{-1} \text{ }^\circ\text{C}^{-1}$ (MatWeb, 2018).

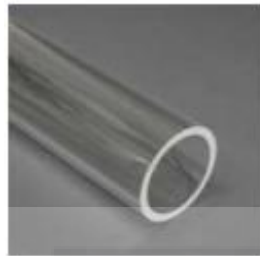


Figure 3.5: Resonator of Thermoacoustic Refrigerator

(Retrieved from: <https://www.eplastics.com/Plastic/plexiglass-cast-acrylic-tubing/ACRCAT2-375ODX-250>)

The initial planning is to make a 1 m (quarter wavelength) resonator that operates under frequency of 86.75 Hz. However, by considering the portability factor, it is considered as too long and therefore, it needs to be cut down to a shorter length of 0.65 m (quarter wavelength). This corresponds to an operation parameter of 133.46 Hz of flow frequency. The acoustic wave number, J is therefore changed from 1.57 m^{-1} to 2.42 m^{-1} .

3.2.1.3 Loudspeaker

The sound driver used in the thermoacoustic refrigerator is a used car loudspeaker of Hyundai i10 2008. The loudspeaker's maximum power is 300 W (Amazon, 2018). Figure 3.6 shows the loudspeaker that is used in the thermoacoustic refrigerator rig.



Figure 3.6: Sound Driver for Thermoacoustic Refrigerator

3.2.1.4 Stack

The cross-section of the 3D printed stack is as shown in Figure 3.7. Its area is 5.04 cm² which gives a porosity of 0.3326. The acoustic wave number is calculated by formula, $J = 2\pi / \lambda$ and for a resonator with a 0.65 m long (quarter wavelength), the acoustic wave number, J is 2.42 m⁻¹. The porosity is low due to inability to adjust the thickness of the printed plate because of the limitation of CubePro nozzle as the minimum thickness is 1.2 mm. According to Zolpakar et al (2016), given that the parameters of the stack are as below:

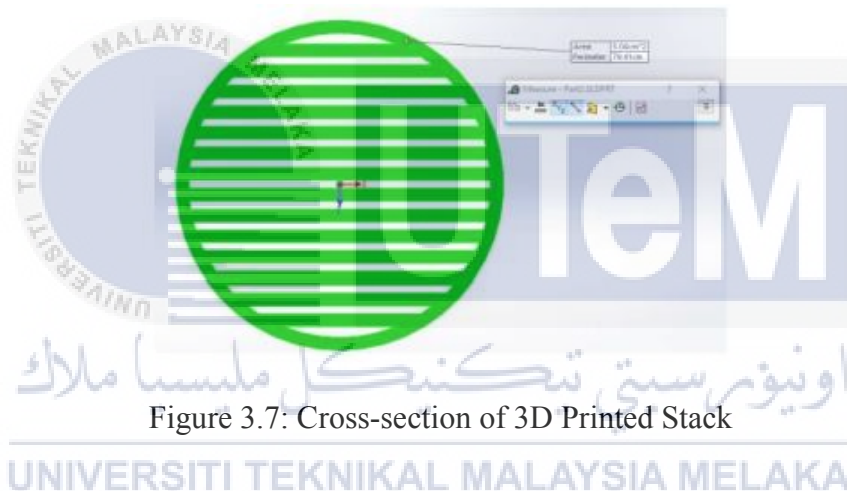
$$0 \leq L_{sn} \leq 1$$

$$0.06 \leq x_{sn} \leq 0.42$$

$$0.67 \leq B \leq 0.8$$

$$0.015 \leq D \leq 0.03$$

From the parameters above, the stack length, L_s , stack center position x_s , porosity, B and drive ratio, D should be $0 \leq L_s \leq 0.414$ m, 0.025 m $\leq x_s \leq 0.174$ m, $0.67 \leq B \leq 0.8$ and $0.015 \leq D \leq 0.03$ respectively. The stack length, L_s is 0.04 m, stack center position, x_s is 0.42m and porosity, B is 0.3326. Thus, the stack of the thermoacoustic refrigerator is not yet optimized because the stack is initially designed for 1 m (quarter wavelength) resonator which operates in 86.75 Hz frequency and has 1.57 m⁻¹ acoustic wave number but due to the inconveniences to transport the rig, the resonator is then cut shorter and the operation parameters are adjusted accordingly.



Two types of stacks are selected in the experiment to compare their efficiency on the temperature change between two ends of the stack. The first stack is made of Acrylonitrile Butadiene Styrene (ABS) by using three dimensions (3D) printer. A Computer Aided Drawing (CAD) software, SolidWorks was used with associated to make the stack for the thermoacoustic refrigerator. Then, the drawn stack in SolidWorks is then saved as stereolithography (STL) format so that it can be sliced in the Cubepro software for 3Dprinting.

Cubepro software is a software associated with Cubepro 3D printer to do slicing on STL format drawing to give the instruction to the printer before the digital data is transferred to the printer for printing. According to Engineering ToolBox (2005), Acrylonitrile Butadiene Styrene (ABS) material has thermal conductivity, k of $0.195 \text{ W m}^{-1} \text{ K}^{-1}$ and specific heat, C_p of $1420 \text{ J kg}^{-1} \text{ }^\circ\text{K}^{-1}$.

However, due to nozzle limitation of Cubepro 3D printer, the thickness of the stack plate printed must be made in the range of 1.0 mm to 1.2 mm, causing the blockage ratio of $0.67 < B < 0.8$ unable to be achieved. Figure 3.8 (a) shows the 3D printed stack with plate thickness of 1.2 mm, stack length of 4 cm and spacing of 0.75 mm which the parameters give a blockage ratio, B of 0.3326 according to Figure 3.7. Figure 3.8 (b) shows the picture of stainless-steel scrubber stack.

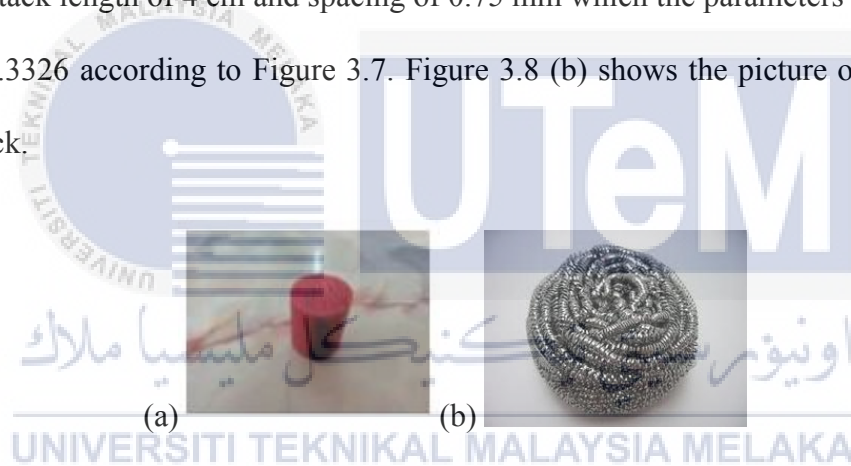


Figure 3.8: (a) 3D-Printed Stack and
(b) Stainless-Steel Scrubber Stack

The top of the resonator is sealed with a Cubepro 3D-printed cover which uses the same materials as the stack, and it is printed with the 3D-printed stack.

Since the 3D-Printed ABS material and stainless-steel scrubber material are coming from manufacturer without specified thermal properties, their specific heat, C_p , and thermal conductivity, k are assumed as $1420 \text{ J kg}^{-1} \text{ K}^{-1}$, and $0.195 \text{ W m}^{-1} \text{ K}^{-1}$ respectively for ABS stack which is following to the properties from Table 2.2 while $500 \text{ J kg}^{-1} \text{ K}^{-1}$, and $15 \text{ W m}^{-1} \text{ K}^{-1}$ respectively for stainless-steel scrubber (JTE Stainless Steel, n. d.). The porosity of stainless-steel scrubber is assumed as 0.748.

3.2.1.5 Cover

Figure 3.9 shows the figure of 3D printed Acrylonitrile Butadiene Styrene (ABS). The build settings are the same as the 3D printed stack as stated in section 3.2.1.4 which are $200 \mu\text{m}$ layer thickness, solid print strength and honeycomb print pattern.



Figure 3.9: Cover for Thermoacoustic Refrigerator Resonator

Since the cover is made of ABS, it has the same thermal properties as the stack in which thermal conductivity, k is $0.195 \text{ W m}^{-1} \text{ K}^{-1}$ and specific heat, C_p is $1420 \text{ J kg}^{-1} \text{ }^\circ\text{K}^{-1}$. The center of the cover is drilled to form a hole in order to insert measuring tools for measurement and data collections.

3.2.1.6 Amplifier

The amplifier used in this thermoacoustic refrigerator apparatus is Flepcher FLPMT1201. Table 3.3 shows the specification of Flepcher FLP-MT1201 while Figure 3.10 shows the figure of the Flepcher FLP-MT1201 amplifier.



Figure 3.10: Flepcher FLP-MT1201

The amplifier is connected to function generator in order to amplify the acoustic wave in the resonator so that the dynamic pressure, p_o can produce enough drive ratio.

Table 3.3: Specification of Flepcher FLP-MT1201 Amplifier

(Retrieved from: <https://www.flepcher.com/flpd/MT1201.pdf>)

Power Output Level	1kHz, THD + N = 0.1%
RMS @ 8 Ohm Stereo	1200 + 1200W
RMS @ 4 Ohm Stereo	1650 + 1650W
RMS @ 8 Ohm Bridge	3300W
RMS @ 4 Ohm Bridge	3800W
Frequency Response	20Hz – 20kHz \pm 1dB
S/N Ratio	95dB
Slew Rate	$\geq 25V/\mu s$
Phase Response	$\pm 10^\circ$
Damping Factor (8Ohm, 1f-1kHz)	650
Line Input	240V, 50Hz
Input Connectors	Female XLR + Male XLR
Dimension (W X D X H)	482 X 483 X 132
Weight	41 kg

3.2.1.7 Function Generator

The function generator used in the thermoacoustic refrigerator apparatus is MCP SG1005 as shown in Figure 3.11. Table 3.4 shows the specification of MCP SG1005 function generator. The function generator is connected to a loudspeaker and an amplifier by Bayonet Neil Concelman (BNC) cables. There are 2 cables which are BNC head to BNC tail cable and BNC head to 2 branch tails cable.

Table 3.4: Specification of MCP SG1005 Function Generator

(Retrieved from: https://mcpsh.en.alibaba.com/product/287091019-212404941/SG1005_digital_function_signal_generator.html)

Technical Data	SG1005	
Data Main Output	Output frequency	0.1 Hz ~ 5 MHz
	Output amplitude	0.2 ~ 20 V_{p-p}
	Output waveform	Sine, square, triangle
	Amplitude accuracy	$\pm 10\%$ (1 kHz, 20 V_{p-p})
	Frequency accuracy	$\pm 5 \times 10^{-6}$
	Frequency resolution	100 mHz
	Frequency stability	$\pm 1 \times 10^{-6}$
	Impedance	50 $\Omega \pm 10\%$
	Attenuator	-40dB, 0dB
	Display	6 digits LED display
	Output control	ON/OFF selector
	DC offset	± 10 V

Sine wave	Distortion factor	$\leq 0.3\%$ (20 Hz ~ 20 kHz)
Square wave	Rise or fall time	≤ 25 ns
	Duty cycle	10% ~ 90%
Triangle wave	Linear	$\geq 98\%$ 100 mHz ~ 100 kHz
		$\geq 95\%$ 100 kHz ~ 1 MHz
TTL/COMS output	TTL level	$\geq 3 V_{p-p}$
	Output Capability	20TTL Load
	CMOS level	3 ~ 13.5 V_{p-p}
Power supply		220 ~240 V _{AC} \pm 10%,
Dimension (WxHxD)		300 x 110 x 265 mm
Weight		1.5 kg

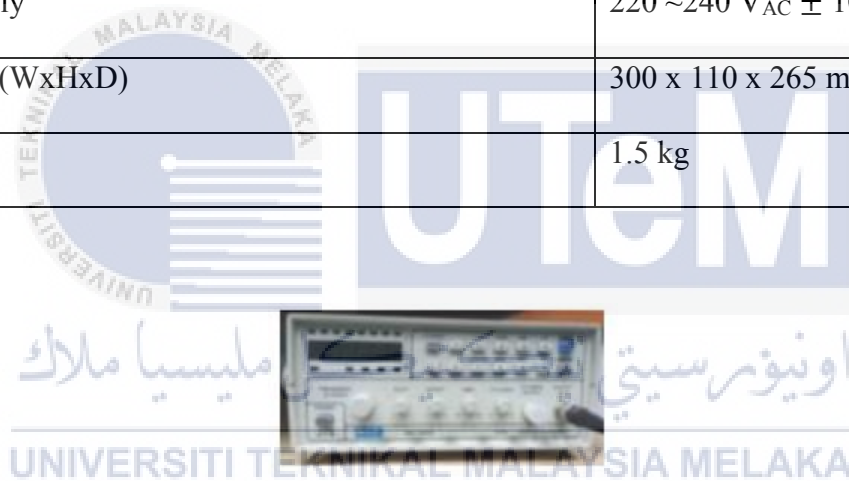


Figure 3.11: MCP SG1005 Function Generator

The MCP SG1005 function generator is used to adjust the frequency of the loudspeaker to 133.45 Hz so that the loudspeaker vibrates according to a frequency of 133.45 Hz.

3.2.2 Fabrication and Assembling

The fabrication tool used in fabricating the thermoacoustic refrigerator apparatus are the table saw, a handrail and a 3 mm drill bit. The handrail is used to drill a 3 mm hole with 3 mm drill bit on the loudspeaker box. The acrylic box is labelled by marking on a paper marking tape with permanent marker pen first before drilling starts. Then, a wood is placed at the bottom of the acrylic box is placed a wood to prevent the excessive drilling force from handrail to crack the box. Table saw is used to cut the acrylic tube and the wood to a desired dimension of 40 cm x 100 cm wood for placing the apparatus and 0.65 cm acrylic tube as resonator. Then flat heat cross screw with 1 cm long is used to screw the acrylic box onto the wood.

The acrylic tube is glued with acrylic box by V-Tech Acetic Silicone using silicone gun. Figure 3.12 shows the figure of V-Tech Acetic Silicone.

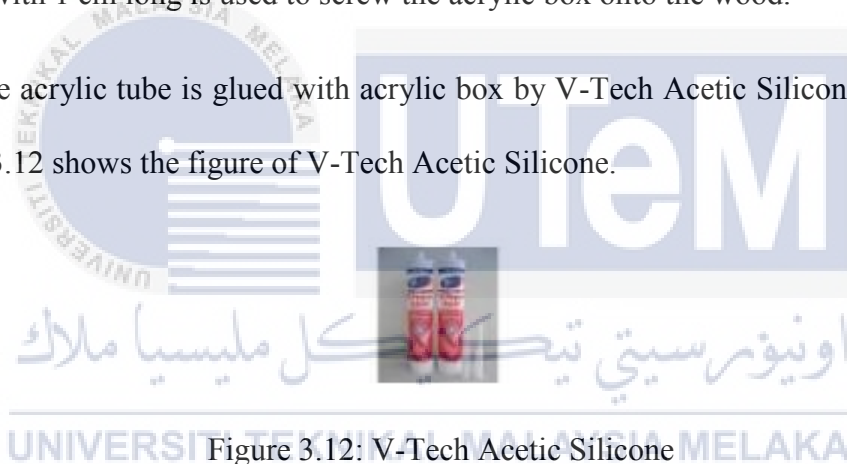


Figure 3.12: V-Tech Acetic Silicone

(Retrieved from: [https://shopee.com.my/V-tech-Acetic-silicone-All-purpose-sealant-Versatilesealant-\(Indoor-Outdoor\)-i.13517183.347249048](https://shopee.com.my/V-tech-Acetic-silicone-All-purpose-sealant-Versatilesealant-(Indoor-Outdoor)-i.13517183.347249048))

There are four M4 x 0.7 x 50 button head cap screws and twelve M4 hex bolt nuts used to lock the loudspeaker rigidly. Figure 3.13 (a) and 3.13 (b) show the image of the screws and nuts used in assembling the loudspeaker respectively.

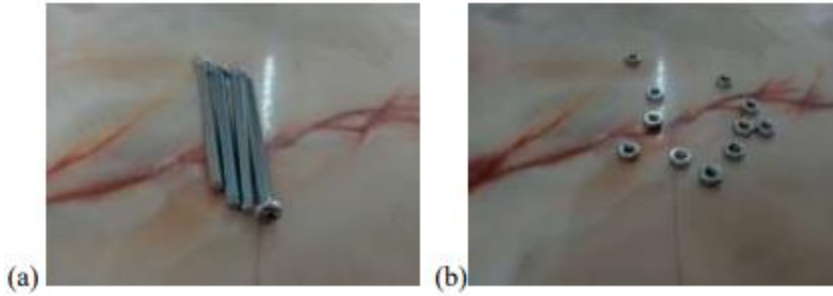
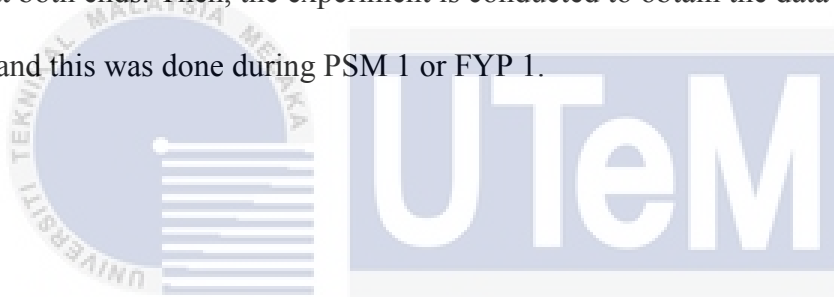


Figure 3.13: (a) M4 Screws and (b) M4 Bolt Nuts

Thermocouple is being installed at both ends of the stack in order to obtain the temperature at both ends. Then, the experiment is conducted to obtain the data for the temperature, and this was done during PSM 1 or FYP 1.



3.2.3 Calibration and Debugging

The instruments used to measure the temperature and velocity of the thermoacoustic standing wave inside the resonator are PicoLog Data Logger TC 08 with association with PicoLog 6 software and SENTRY ST-730 hot wire as shown in Figure 3.14 and Figure 3.15 respectively.



Figure 3.14: PicoLog Data Logger TC 08



Figure 3.15: SENTRY ST-730 Hot Wire



اونيورسيتي تيكنيكل مليسيا ملاك

UNIVERSITI TEKNIKAL MALAYSIA MELAKA

The thermocouple used is type K thermocouples as shown in Figure 3.15. The hot wire is used to calibrate the thermocouple readings. It is found that the type K thermocouples offset at 1.6 °C for the blue thermocouple and 1 °C for the orange thermocouple as shown in Figure 3.16.



Figure 3.16: Type K Thermocouples

3.2.4 Summary of Thermoacoustic Refrigerator

Thermoacoustic refrigerator as shown earlier in Figure 3.2 was used for implementing an experiment. The operating parameters, gas parameters and stack parameters for thermoacoustic refrigerator's parameters are summarized and listed in Table 3.5 for three-dimensional (3D) acrylonitrile butadiene styrene (ABS) printed stack and Table 3.6 for stainless-steel scrubber stack. The calculation is based on the formulas in chapter 2.

As suggested by Zolpakar et al. (2016). Most of the operating parameters are according the optimized criterias. However, due to limitation of CubePro 3D printer, the plate thickness was set to 1.2 mm. Next, the ABS and stainless-steel scrubber materials are supplied by manufacturer without any specification details. Their thermal properties in terms of specific heat, C_p and thermal conductivity, k are therefore assumed to be the same as the thermal properties which are found in the website and the resources are described in subsection 3.2.1.4.

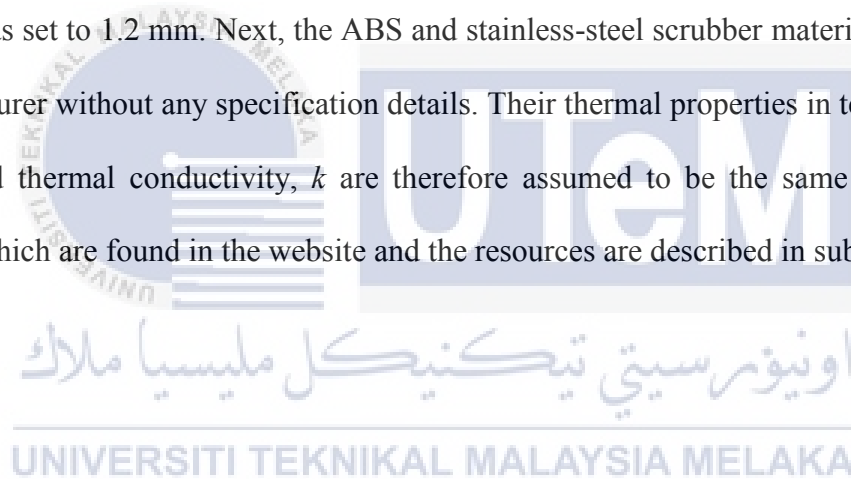


Table 3.5: Thermoacoustic Refrigerator's Parameter (3D-Printed ABS Stack) Summary

Operating Parameters		Gas Parameters	
Quarter Wavelength, $\lambda / 4$	0.65 m	Speed of Sound, a	347 m s ⁻¹
Wavelength, λ	2.6 m	Thermal Conductivity, k	0.02566 W m ⁻¹ K ⁻¹
Acoustic Wave Number, J	2.42 m ⁻¹	Thermal Penetration Depth, δ_k	0.233 mm
Frequency, f	133.45 Hz	Specific Heat, C_p	1007 J kg ⁻¹ K ⁻¹
Mean Pressure, P_m	101 kPa	Mean density, ρ_m	1.176 kg m ⁻³
Mean Temperature, T_m	300 K	Gas Displacement, ζ	0.47 m
Stack Parameters (ABS)			
Stack Length, L_s			0.04 m
Stack Center Position, x_s			0.43 cm
Thermal Conductivity, k			0.195 W m ⁻¹ K ⁻¹
Specific Heat, C_p			1420 J kg ⁻¹ K ⁻¹
Spacing, $2y_o$			0.75 mm
Plate Thickness			1.2 mm
Stack Diameter, d_i			3.1 cm
Porosity, B			0.3326

Table 3.6: Thermoacoustic Refrigerator's Parameter (Stainless Steel Scrubber Stack)

Summary

Operating Parameters		Gas Parameters	
Quarter Wavelength, $\lambda / 4$	0.65 m	Speed of Sound, a	347 m s ⁻¹
Wavelength, λ	2.6 m	Thermal Conductivity, k	0.02566 W m ⁻¹ K ⁻¹
Acoustic Wave Number, J	2.42 m ⁻¹	Thermal Penetration Depth, δ_k	0.233 mm
Frequency, f	133.45 Hz	Specific Heat, C_p	1007 J kg ⁻¹ K ⁻¹
Mean Pressure, P_m	101 kPa	Mean density, ρ_m	1.176 kg m ⁻³
Mean Temperature, T_m	300 K	Gas Displacement, ζ	0.47 m
Stack Parameters (ABS)			
Stack Length, L_s			0.12 m
Stack Center Position, x_s			0.53 mm
Thermal Conductivity, k			15 W m ⁻¹ K ⁻¹
Specific Heat, C_p			500 J kg ⁻¹ K ⁻¹
Stack Diameter, d_i			3.1 cm
Porosity, B			0.748

3.3 Computational Fluid Dynamics (CFD) Simulation

3.3.1 Geometry Drawing

The geometry model is drawn based on the cross-section of the three dimensional (3D) printed acrylonitrile butadiene styrene (ABS) with a resonator of quarter wavelength of 0.65 m which is functioning under 133.5 Hz of frequency. Due to limited time to complete PSM II, two-dimensional (2D) simulation analysis is selected instead of 3D simulation analysis. Figure 3.17 shows the geometry drawing in ANSYS drawing. The cylindrical resonator is in 31 mm diameter and 0.65 m length.

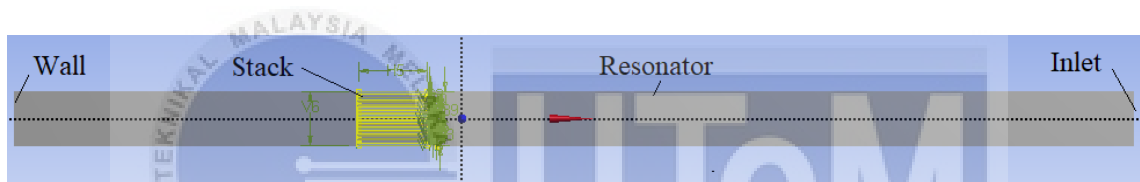


Figure 3.17: 2D Geometry Drawing in ANSYS

Figure 3.18 shows the dimension at the stack's area. The colored rectangle as labelled "C" is the stack plates with thickness of 1.2 mm for each plate while the label "B" that is laid between the plates is the gap with 0.75 mm spacing. Part "A" is the gaps of top and bottom with 2 mm spacing which is the remaining space for the gaps. The geometry is drawn starting from the origin to the negative x direction.

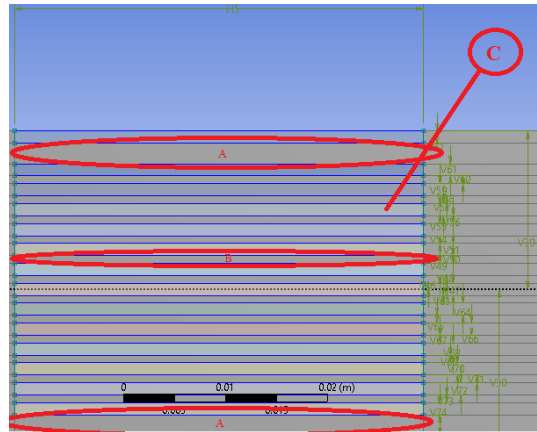


Figure 3.18: Geometry Dimension Parameters

There are two domains of this geometry which are fluid and solid. The fluid part represents the region for the air while the solid part represents the ABS material. The stack center position is at 0.43 m from the inlet, the stack length is at 4 cm where the value is done according to the optimization research by Zolpakar et al. (2016).

Lines are drawn as shown in Figure 3.17 so that the fluid region is divided according to the stack plate position for the purpose of getting good meshing quality. “Face Split” tools is used for the face split by selecting the face as “Target Face” and the lines as “Tool Geometry” in ANSYS geometry drawing. The stack body that is created from the geometry “Add Frozen” extrusion is divided into 15 parts where each part represents a single stack plate while the fluid region created by “Add Material” extrusion remain as one part.

Next, “Boolean” is used by using “Subtract” operation with preserve tool body “Yes” and the target body is the fluid while the tool bodies are all the stack body. All of the bodies are combined into one part before proceeding with meshing. The fluid body is set as “Fluid” body while the stack bodies are set as “Solid” body in the details of the surface body.

3.3.2 Meshing

In this section the meshing for the geometry as mentioned in section 3.3.1 will be discussed. There are two types of meshing methods used in the ANSYS meshing tool such as “Edge Sizing” and insertion mesh method of “MultiZone Quad/Tri”. Figure 3.19 shows the respective applied edges with the added methods. As in Figure 3.19, “Edge Sizing” is applied on the edges of every 0.75 mm stack gaps while “Edge Sizing 6” is applied on the top and bottom edges which is 2 mm gap. The “MultiZone Quad/Tri” is applied on the whole geometry including the fluid and solid parts.

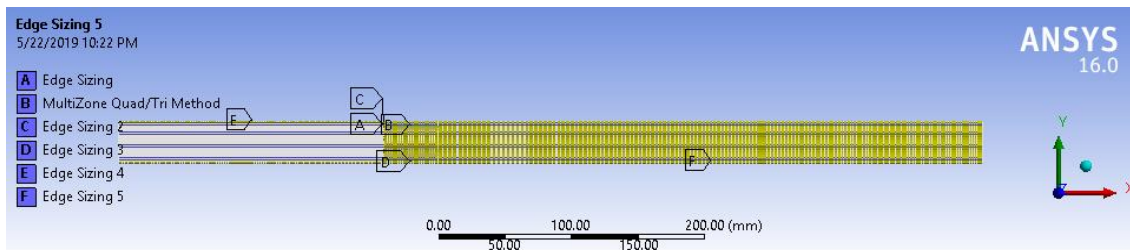


Figure 3.19: Meshing Methods Used in ANSYS Meshing

“Edge Sizing 2” is applied on all the stack plate edges of 1.2 mm thickness while “Edge Sizing 3” is applied along the stack’s length of 4 cm. The inlet begins from $x = 0.39$ m to the right side until $x = -0.26$ m. The left-side end boundary is named as “inlet” boundary while the right-side end boundary is set as “wall boundary” since the resonator has no outlet flow. Both lines starting from coordinate (0.39, 15.5) and coordinate (0.39, -15.5) to (-0.26, 15.5) and (-0.26, -15.5) respectively in meter are named as “resonator wall” in the named selection. “Edge Sizing 4” is applied on all parallel horizontal lines starting from x position, $x = -0.06$ m from y -axis to the end of right wall boundary and “Edge Sizing 5” is applied on all parallel horizontal lines from $x = -0.02$ m to the inlet boundary.

Table 3.7 shows details on all of the edge sizing that is applied in the ANSYS meshing as mentioned above while Table 3.8 shows the details on the inserted meshing method “MultiZone Quad/Tri”.

Table 3.7: Details on Edge Meshing in ANSYS Meshing

Sizing Name	Number of Edges	Number of Divisions	Behavior	Bias Type	Bias Factor
Edge Sizing	14	15	Hard	-----	2
Edge Sizing 2	15	3	Hard	No Bias	-
Edge Sizing 3	30	20	Hard	-----	1
Edge Sizing 4	30	120	Hard	-----	2
Edge Sizing 5	30	150	Hard	-----	2

Table 3.8: Details on “MultiZone Quad/Tri” Inserted Mesh Method

Definition	
Suppressed	No
Method	MultiZone Quad/Tri
Surface Mesh Method	Program Controlled
Element Midside Nodes	Use Global Setting
Free Face Mesh Type	Quad/Tri
Advanced	
Preserve Boundaries	Protected
Mesh Based Defeaturing	On
Defeaturing Tolerance	Default (1.6127e-002 mm)
Sheet Loop Removal	No
Minimum Edge Length	0.75 mm
Write ICEM CFD Files	No

Figure 3.20 shows the meshed display around the stack’s zone while Figure 3.21 shows named selections for each boundary that is defined as “inlet”, “wall” and “resonator”. With reference to Table 3.8, the number of divisions are required to be high to produce many nodes especially for the stack’s gaps since the gaps is the key element to make thermoacoustic effect happens.

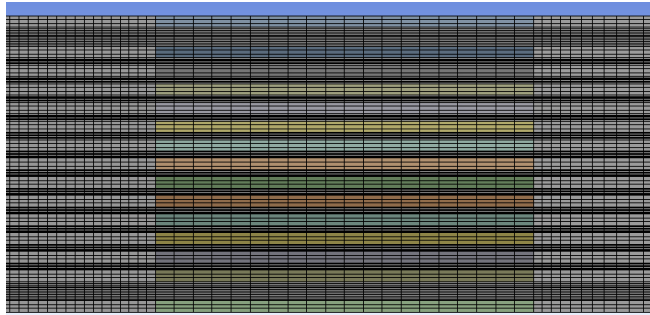


Figure 3.20: Zoom in View of Mesh Display At Stack's Zone

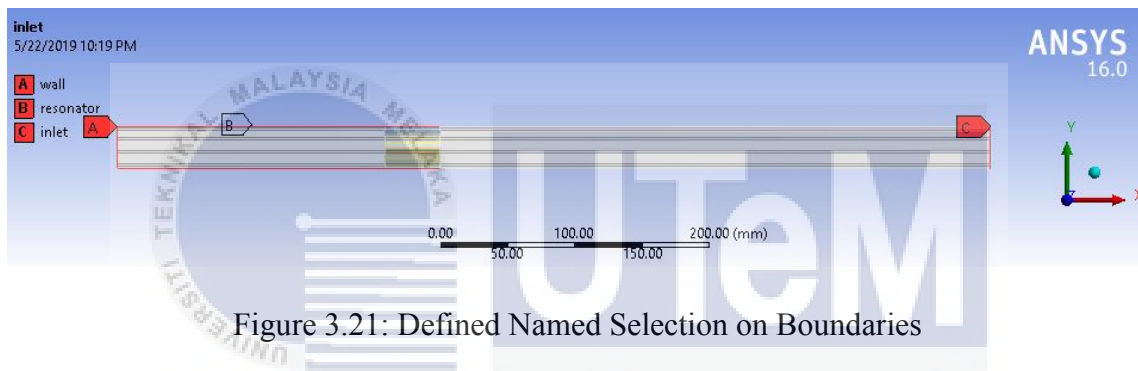


Figure 3.21: Defined Named Selection on Boundaries

The boundaries are defined with “Named Selection” before proceeding with simulation setup. Un-named selections or boundaries will be automatically named as interior body, shadow body, surface body, et cetera.

3.3.3 Mesh Checking

After saving and updating the meshing of the model as discussed in section 3.3.1 to section 3.3.2, simulation setup is started to be proceeded with double precision 2D setup. Figure 3.22 and Figure 3.23 show the mesh size and mesh quality, respectively, for the model.

```
Mesh Size

Level    Cells    Faces    Nodes    Partitions
  0      37410    75889    38478    1

16 cell zones, 52 face zones.
```

Figure 3.22: Mesh Size

The mesh size and mesh quality of model can be checked by selecting the “Mesh” toolbar options and then clicking “Quality” and “Size” from “Info” tab in ANSYS setup.

```
Mesh Quality:
Minimum Orthogonal Quality = 1.00000e+00
(Orthogonal Quality ranges from 0 to 1, where values close to 0 correspond to low quality.)

Maximum Ortho Skew = 2.98023e-07
(Ortho Skew ranges from 0 to 1, where values close to 1 correspond to low quality.)

Maximum Aspect Ratio = 3.97180e+01
```

Figure 3.23: Mesh Quality

The skewness of the mesh is suggested to be lower than 0.75 while the aspect ratio is suggested to be lower than 16. However, for this mesh model, the skewness is very good, but the aspect ratio is fairly acceptable due to the high number of nodes or number of divisions at the stack's gaps. Since thermoacoustic effect happens in the gaps of the stack and the number of nodes is required to be high so that the fluid can be studied more accurately. But in another hand, with consideration of meshing quality, the number of divisions or nodes are adjusted so that it is not too high. Table 3.9 shows the respective mesh metrics, skewness and aspect ratio for the mesh model.

Table 3.9: Skewness and Aspect Ratio of Mesh Model

Skewness		Aspect Ratio	
Min	1.3058e-010	Min	2.5625
Max	7.0698e-005	Max	39.705
Average	6.8681e-006	Average	12.577
Standard Deviation	1.299e-005	Standard Deviation	8.2385

3.3.4 Solver Setting

Figure 3.24 shows the general setting of the simulation setup where the solver is pressure-based, absolute velocity formulation, transient time, and planar two-dimensional (2D) space with gravitational acceleration acted on negative y direction, $g = -9.81 \text{ m s}^{-2}$ and floating operating pressure of 101,325 Pa. In the models' material setup, there are two materials such as air and acrylonitrile butadiene styrene (ABS) in this simulation.

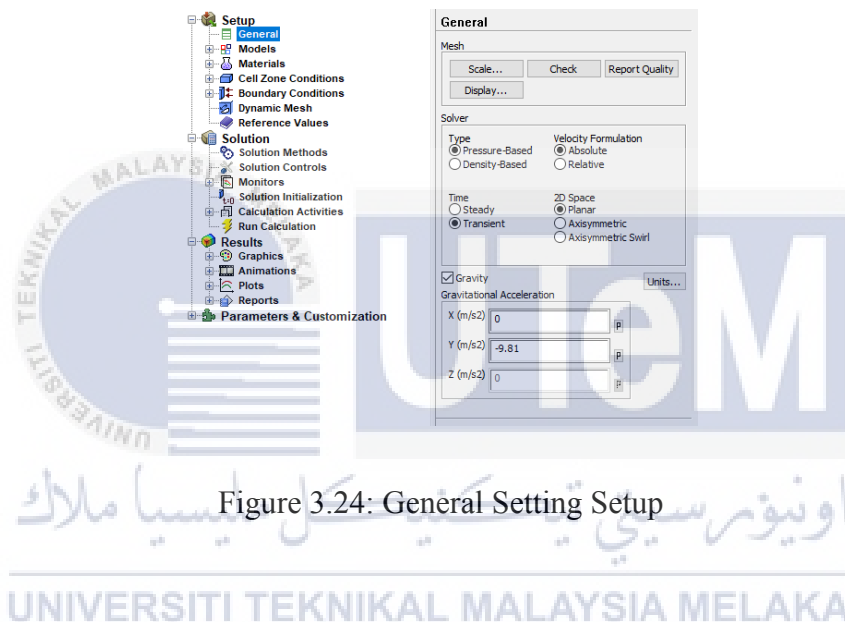


Figure 3.24: General Setting Setup

Figure 3.25 (a) and Figure 3.25 (b) shows the specific heat, C_p polynomial profile and thermal conductivity, k of air respectively. The specific heat, C_p and thermal conductivity, k are polynomial function as shown in Eq. (3.1) and (3.2) respectively. The correlation coefficient, R^2 of Eq. (3.1) and (3.2) are 0.99961 and 0.99993 respectively. The viscosity is set as power-law. The density, ρ , specific heat, C_p , and thermal conductivity, k of ABS are 1215 kg m^{-3} , $1.42 \text{ kJ kg}^{-1} \text{ K}^{-1}$, and $0.195 \text{ W m}^{-1} \text{ K}^{-1}$ respectively. The air is set as ideal gas for this case and T is the temperature of air.

$$C_p = 1.9327 \times 10^{-10} T^4 - 7.9999 \times 10^{-7} T^3 + 1.1407 \times 10^{-3} T^2 - 4.4890 \times 10^{-1} T + 1.0575 \times 10^3 \quad (3.1)$$

$$k = 1.5207 \times 10^{-11} T^3 - 4.8574 \times 10^{-8} T^2 + 1.0184 \times 10^{-4} T - 3.9333 \times 10^{-4} \quad (3.2)$$

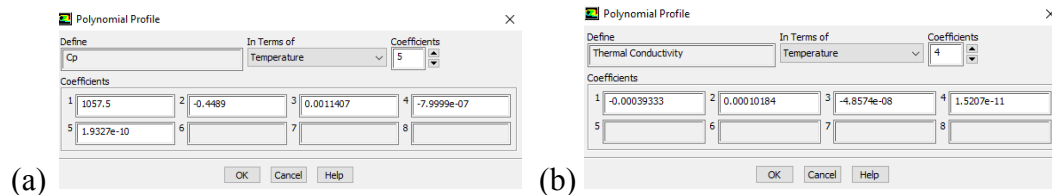


Figure 3.25: (a) Specific Heat Polynomial Profile of Air and

(b) Thermal Conductivity Polynomial Profile of Air

The viscosity of the air is set as power law with three coefficients method. According to Swift (2001), the viscosity and temperature exponent are $1.85 \times 10^{-5} \text{ kg m}^{-1} \text{ s}^{-1}$ and 0.76 respectively. Figure 3.26 shows the power law profile of air.

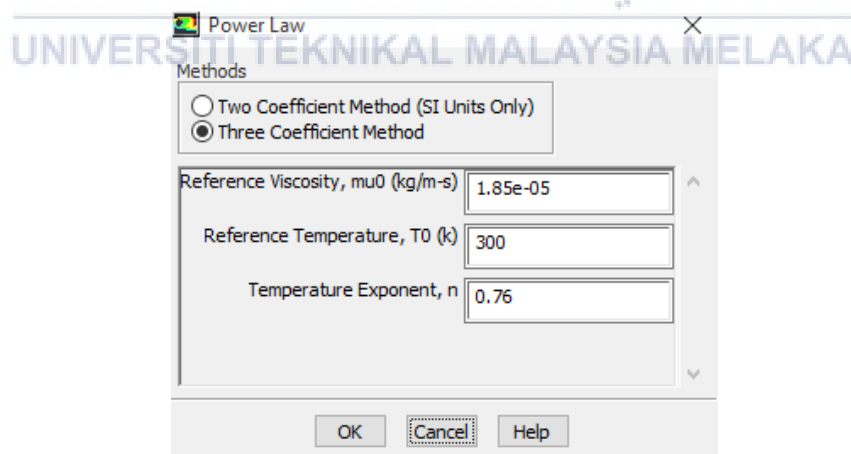


Figure 3.26: Power Law Viscosity Profile of Air

The boundary condition is set as mass flow inlet with mass flux inlet normal to boundary direction. According to Mohd Saat and Jaworski (2013), the inlet pressure and mass flux equations are as shown in Eq. (3.3) and Eq. (3.4). The mass flux is being interpreted by using code in “.c” file extension and the code is as shown in Figure 3.27.

$$P_l = P_a \cos(Jx) \cos(2\pi ft) \quad (3.3)$$

$$m_l = (P_a / c) \sin(Jx) \cos(2\pi ft + \theta) \quad (3.4)$$

where P_l is the inlet pressure, P_a is the antinode pressure, J is the wave number, x is the length of the resonator, f is the frequency of flowing air, t is the time taken, θ is the phase difference, and m_l is the mass flux. However, the inlet oscillating pressure formula is not used in this interpretation because the inlet boundary is defined as mass flux inlet and the formula of mass flux is applied.

```
#include "udf.h"
DEFINE_PROFILE(massfluxin,thread,position)
{
    face_t f;
    real t=CURRENT_TIME;

    begin_f_loop(f,thread)
    {
        F_PROFILE(f,thread,position)=0.588*cos(2513.3*t+1.5708);
    }
    end_f_loop(f,thread)
}
```

Figure 3.27: Mass Flux Code for User-Defined Function

The mass flux is at 0.588 kg m^{-2} amplitude with 90° phase difference to the pressure and frequency of 133.45 Hz . The velocity of the air is measured by the SENTRY hot wire in laboratory which is 0.5 m s^{-1} and it is applied to calculate the mass flux amplitude. Figure 3.28 shows the solution methods configuration in the simulation setup. In the solution methods configuration, Pressure-Implicit with Splitting of Operators (PISO) scheme is used for dealing with large number of time steps as it would run up to more than 1,000-time steps while others are following the default configurations.

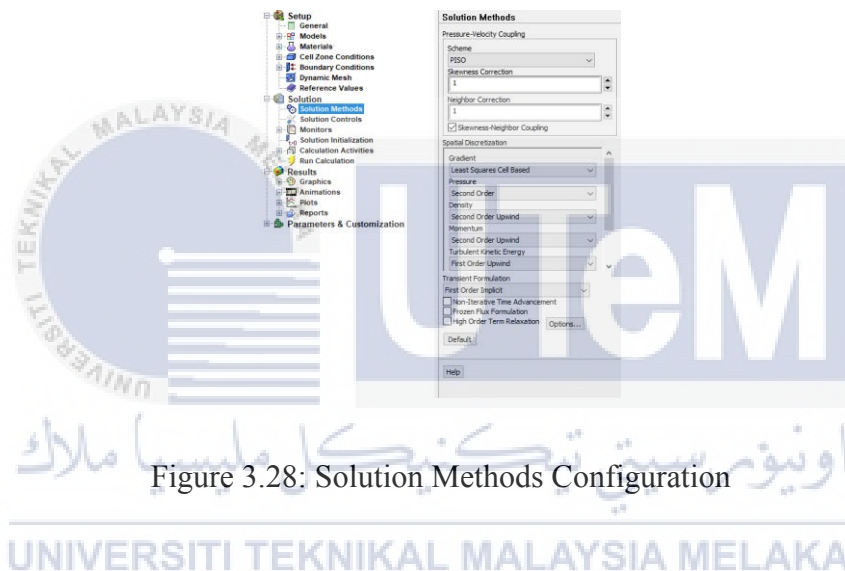


Figure 3.28: Solution Methods Configuration

In the setup, a point surface that is named as “point-52” is created at Cartesian coordinate $(0, 0.065)$ in meter at the middle of the resonator and surface monitor is set on the point for area-weighted average report type. This surface will monitor the simulation and at the same time it records down the x velocity by writing into “v6dv6.out” file and plotting at the setup display as shown in Figure 3.29. This surface is created to check and obtain the axial velocity data for grid independence test & also for the velocity-time analysis of the flow.

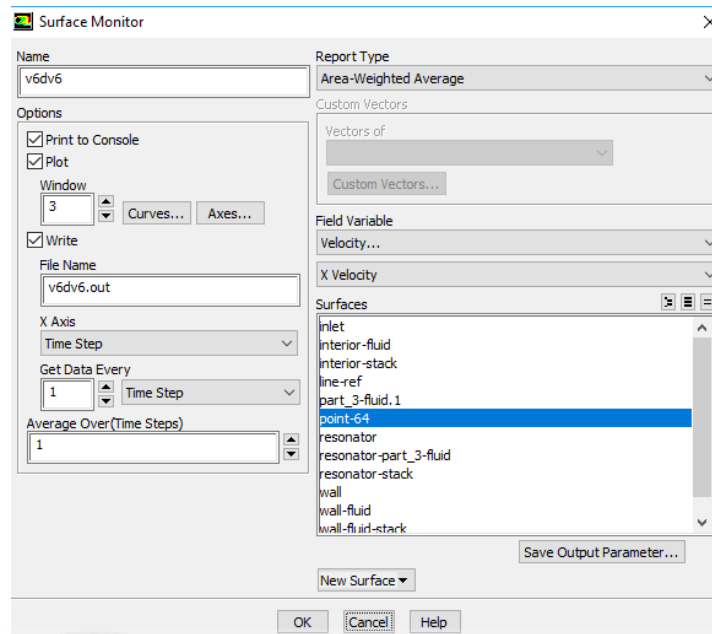


Figure 3.29: Surface Monitor Setting

Calculation is run at 7.5×10^{-6} s of time step size where 1,000 number of time steps is needed to complete one wave cycle for flow frequency of 133.45 Hz and flow period of 7.5 ms. Hence, in order to finish calculating one wave cycle, the simulation has to run for 1,000 time steps. Figure 3.30 shows the “Run Calculation” configuration of the simulation that has been used. Every time step, the maximum iteration is 20 in which the calculation should be converged at iteration of 10 to 20 in every time step.

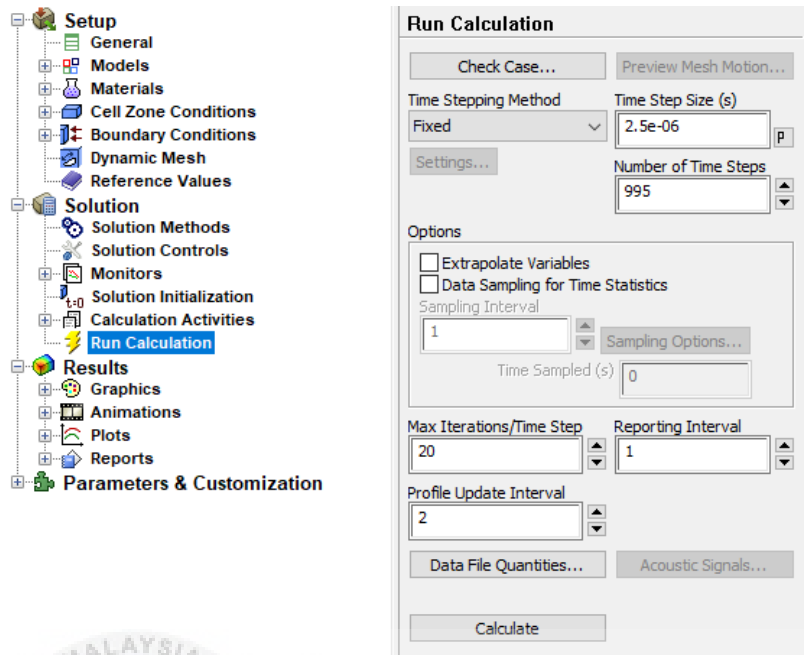
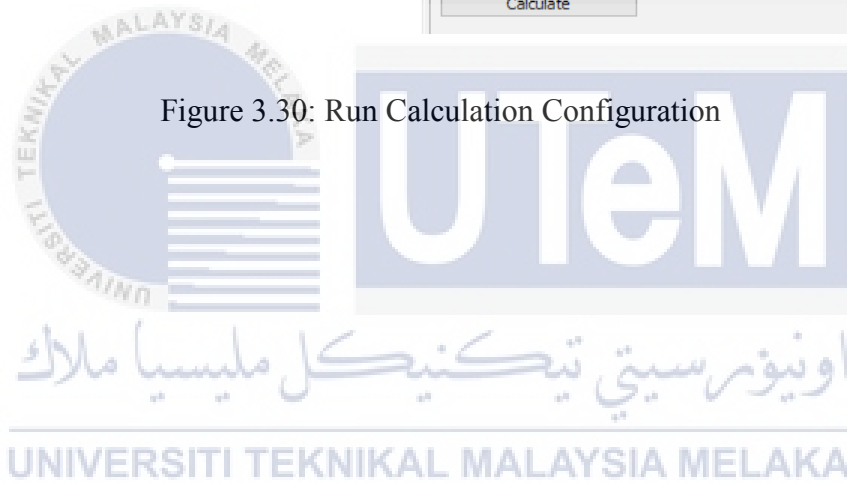


Figure 3.30: Run Calculation Configuration



3.3.5 Grid Independence Test Method

Grid independence test is important to determine whether the results depend on the deviation of the mesh density or not. It is an approach that is used to get a fundamental solution to be independent of either grid size or scale factor. It is tested by running the same setup as described in subsection 3.3.4 and the results are compared for different amount of mesh nodes. The low mesh density is defined as low amount of mesh nodes where the mesh setting is as discussed in subsection 3.3.2 while the high mesh density is the mesh nodes which has doubled number of divisions of all edge sizing as defined in Table 3.7.

In this case study, velocity surface monitor is created which is described in subsection 3.3.4 in Figure 3.29 on a point at the middle of the resonator to obtain the x direction velocity throughout a time period in the simulation. The simulation is run using two different types of mesh density which are described above to obtain two results of x -velocity against time step so that they can be compared. If the difference of both the results are not too high, the model can be said as grid independent model where the mesh node numbers does not necessary affect the result. The result of the grid independency test is to be reported in the next chapter.

3.3.6 Validation Methods

The validation method used in this project is by comparing the theoretical calculated amplitude of x -velocity wave at point-52 (as described in subsection 3.3.4) with the simulated amplitude result of x -velocity wave at the point-52 for the time step interval of 4,988 to 5,981. Every time step represents $7.5 \mu\text{s}$ of actual flow times in the simulation and for every 1,000 time steps, one cycle of the wave is completed. Hence, the time step that is chosen for the validation is at the fifth cycle of the acoustic wave.

For simulated amplitude result of x -velocity at point-52, the data is obtained from the written surface monitor file which is in “.out” format and processed by using Microsoft Excel Office, and values are extracted from the data for time steps interval of 4,988 to 5,981. For calculated amplitude result of x -velocity at point-52, the data is calculated from Eq. (3.4), where mass flux is equal to the product of air density and air velocity, but the x -coordinate value is 0.325 m for the location of the point-52. Instead of using the exact time flow for the phase, it is replaced by the phase for intervals of 0 rad to 6.283 rad. The rest of the parameters in Eq. (3.4) are as same as the operating parameters of the resonator.

CHAPTER 4

RESULTS ANALYSIS AND DISCUSSION

4.1 Experimental Results

4.1.1 Experimental Result for 3D-Printed ABS Stack

In this section, the experimental data that is obtained from the thermoacoustic rig from laboratory is discussed. There are two stacks that are used for the experiment which are acrylonitrile butadiene styrene (ABS) and stainless-steel scrubber and their respective operating parameters are discussed. Figure 4.1 shows graph for temperature at two end points of three-dimension (3D) printed ABS stack against time. The parameter of the resonator and stack are summarized earlier in Table 3.5.

Graph of Temperature Against Time

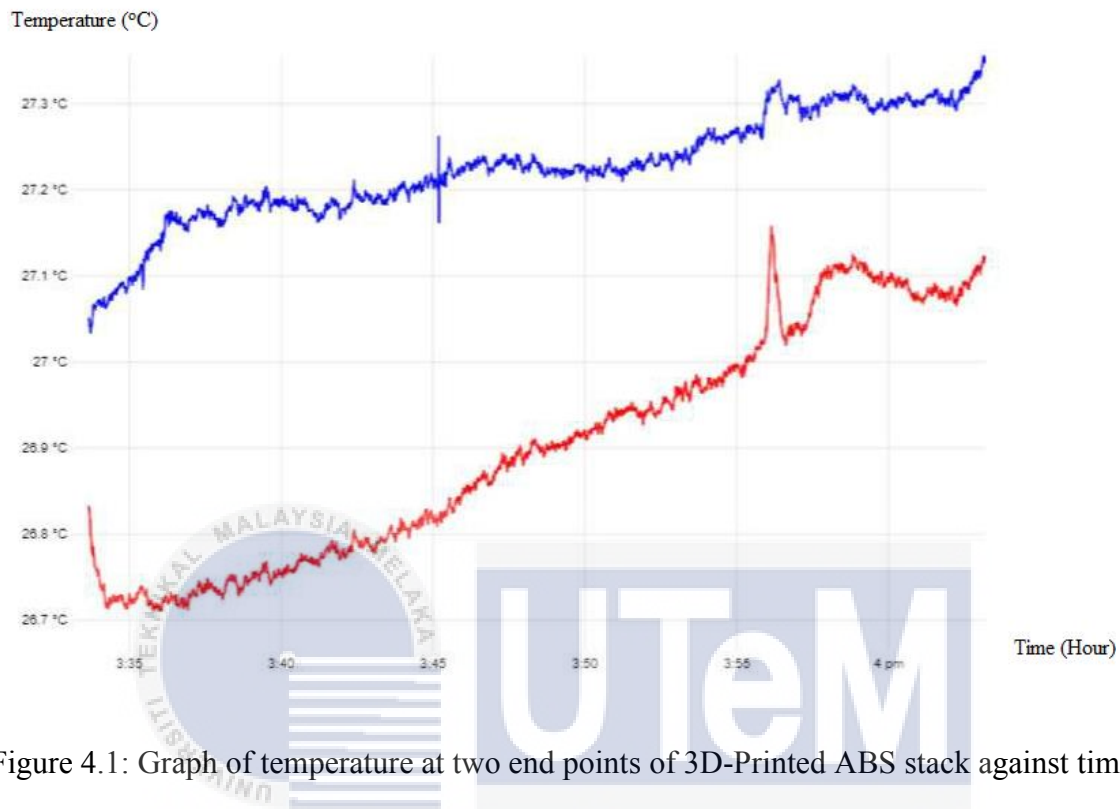


Figure 4.1: Graph of temperature at two end points of 3D-Printed ABS stack against time

The operating, gas, and stack parameters for 3D-printed ABS stack are as shown earlier in Table 3.5. This experimental condition is later being simulated by using computational fluid dynamics (CFD) to obtain pressure drop and velocity data will be discussed in section 4.2.

When ABS stack is used,, the highest temperature gradient recorded is 0.9 °C which was measured using type K thermocouple that is connected to PicoLog TC 08 signal conditioner.

4.1.2 Experimental Result for Stainless Steel Scrubber Stack

Figure 4.2 shows a graph of temperature at two ends of stack against time when the stainless-steel scrubber is used as a stack within the same resonator. The stack is now a 12 cm long stainless-steel scrubber as compared to the earlier used of a 4cm long 3D-printed ABS stack with a stack center position, $x_s = 0.53$ cm.

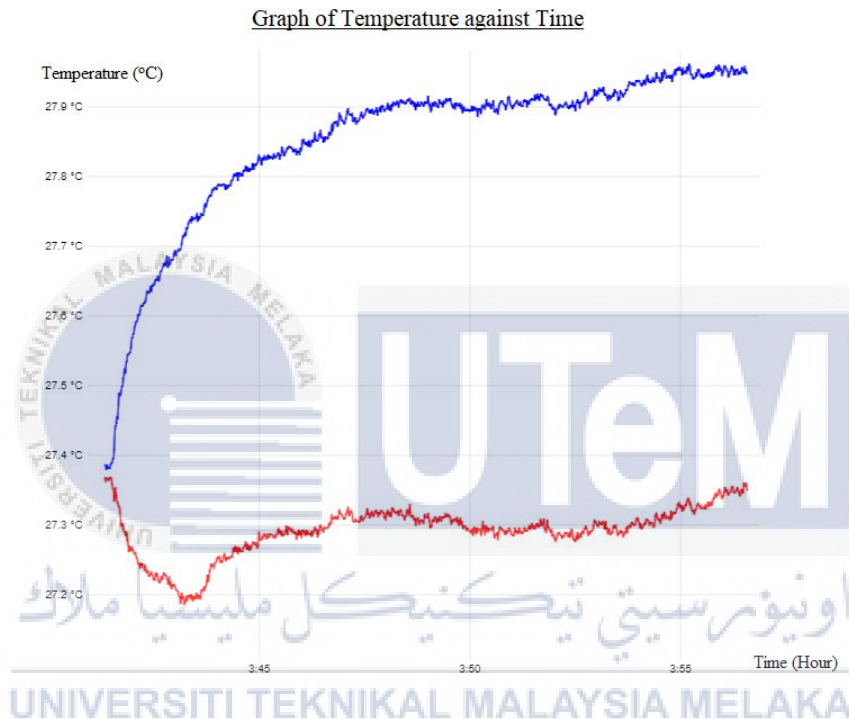


Figure 4.2: Graph of temperature at two end points of stainless-steel scrubber stack against time

The operating, gas, and stack parameter for stainless steel scrubber stack were earlier shown in Table 3.6. The highest temperature gradient recorded using scrubber as stack is 0.6 °C. The curve of the graph against temperature in stainless steel scrubber stack is more stable compared to the 3D-printed ABS stack because the flow is steadier due to higher porosity.

It is shown that the thermoacoustic effect of stainless-steel scrubber stack is more stable than the ABS stack as the graph of temperature against time graph in stainless-steel is more likely uniform than ABS. However, the temperature difference created across the stack is not high enough because optimization of parameters was not been done before the experiment is carried out. Nevertheless, the results show that temperature different was successfully achieved between the two ends of the stack inside the resonator. The temperature different is expected to be bigger if the rig is built at optimum condition (Zolpakar et al., 2017).

4.2 Computational Fluid Dynamics (CFD) Results

Simulation in three-dimensional (3D) mode is expected to offer a much more accurate result than in two-dimensional (2D) mode. However, due to insufficient time to complete the 3D simulation, the CFD simulation was solved using 2D mode in order to obtain the results within the remaining time of the final year project. For different cases of type of stack such as porous medium, complicated geometry, et cetera come with different type of meshing method, this consumes a lot of time especially in the 3D simulation when solving the mesh, setting up the setup, and validating the results. In this subsection, the 2D simulation on the real case of the ABS stack thermoacoustic rig is described.

4.2.1 Grid Independence Test

Grid independency test is important to determine the level of dependency of result with deviation of the mesh density. It is an approach that is used to ensure that the solution is independent of either grid size or scale factor. The grid independency test is done by comparing the results with different mesh density and the methods are described in subsection 3.3.5. Although the result of x -velocity at point-52 (defined in subsection 3.3.4) for low mesh density and high density are similar, the simulation takes longer time to be solved in high density mesh. Velocity changed with time results at the center of the computational domain (point-52) for different mesh density used are as shown in Figure 4.3. The low mesh density is discussed earlier in section 3.3.2 while the high mesh density is the mesh which has doubled number of divisions of all edge sizing. All these information were provided earlier in Table 3.7.

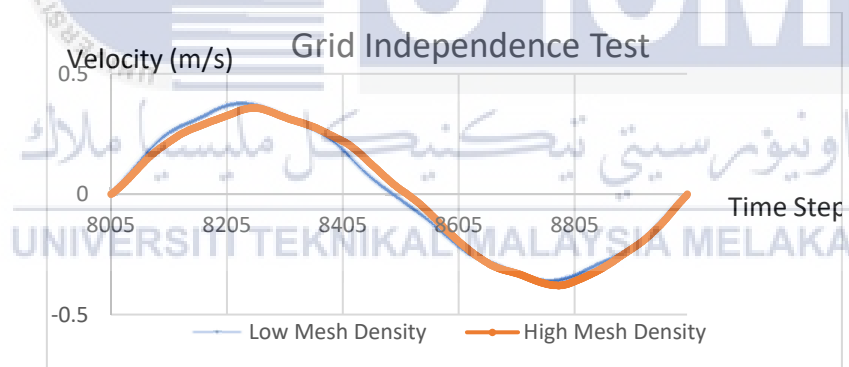


Figure 4.3: x -Velocity at point-52 for different mesh densities

Since the results of x -velocity at point-52 for low mesh density and high mesh density at different phases are the same, the CFD model can be said to be grid independent, and the mesh size will not give significant impact on the results.

4.2.2 Model Validation

After the mesh independency is checked, the simulation is proceeded to next phase, which is verification of the model. The verification method is as described earlier in subsection 3.3.6 and the solver setting is also described earlier as can be found in subsection 3.3.4. Since the amplitude of velocity at the inlet is experimentally measured as 0.5 m s^{-1} , the antinode pressure, P_a can be obtained from calculation and it is found to be 204.04 Pa by using the equations Eq. (3.3) and Eq. (3.4). Therefore, the drive ratio is 0.2% for the resonator apparatus that functioned at a frequency of 133.45 Hz and a length of the 0.65 m of the quarter wavelength. Figure 4.4 shows the x -velocity comparison between the simulated and calculated amplitude results at point-52.

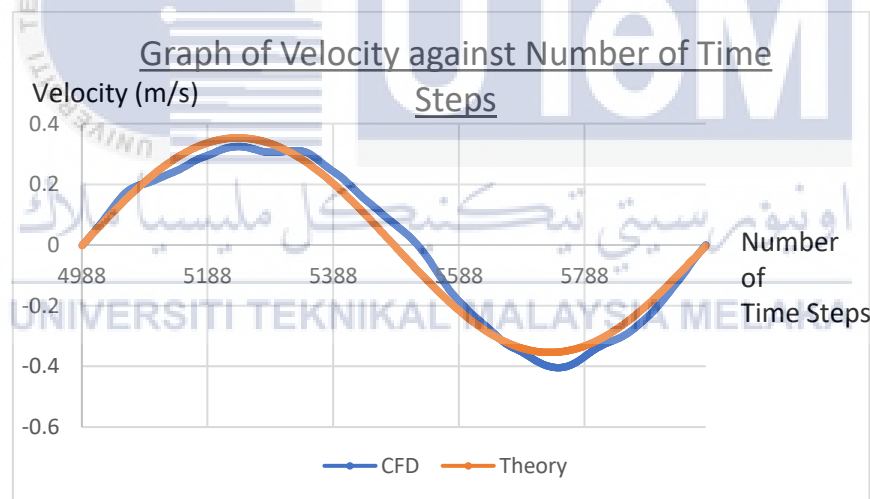


Figure 4.4: Comparison of x -velocity of point-52 between the theoretical and simulation results

Table 4.1 shows the percentage of error by comparing the theoretical calculated result and the simulated result.

Table 4.1: Percentage of error of amplitude

Amplitude	Theoretical Value (m s ⁻¹)	Simulation Value (m s ⁻¹)	Percentage of Error (%)
Maximum	0.324752	0.35372	8.15
Minimum	-0.40379	-0.35357	14.20

In general, a good match is found between the results from theoretical predictions and the CFD models. The x -velocity at point-52 from the model is fluctuating along the time steps, and the direction is changing repeatedly from left to right and right to left. This is due to the sinusoidal characteristic of the acoustic wave based on thermoacoustic principle.

4.2.3 Pressure Result

The pressure contour of the resonator is captured when the wall boundary pressure reached an antinode pressure value of 218.88 Pa that is at 7,768 time steps which is also 14.84 Pa higher than the theoretically calculated antinode pressure as described in subsection 4.2.2 which is 204.04 Pa. In the theoretical pressure calculation, there is no consideration on the presence of stack but in actual case, the pressure of the air particles increases when it passes through the stack, causing the increase of pressure in the wall boundary. Figure 4.5 shows the pressure contour result from the CFD simulation with the presence of stack.

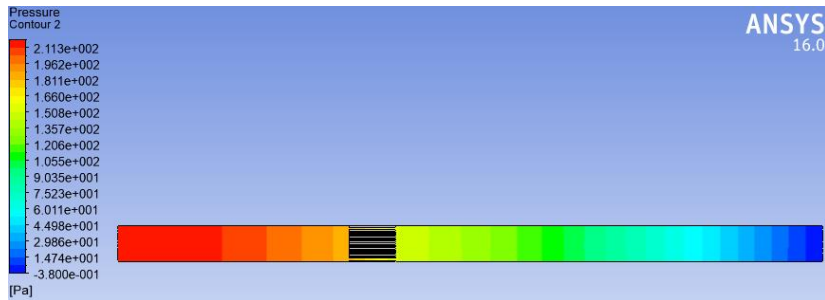


Figure 4.5: Pressure contour result from CFD Simulation

A graph of pressure against x direction is plotted as shown in Figure 4.6. The maximum temperature at the antinode is 218.88 Pa and if it is compared to the theoretical calculation, it has increased for 7.27%. Hence, the air particles are vibrating in range of 0 Pa to 218.88 Pa of pressure in the resonator environment.

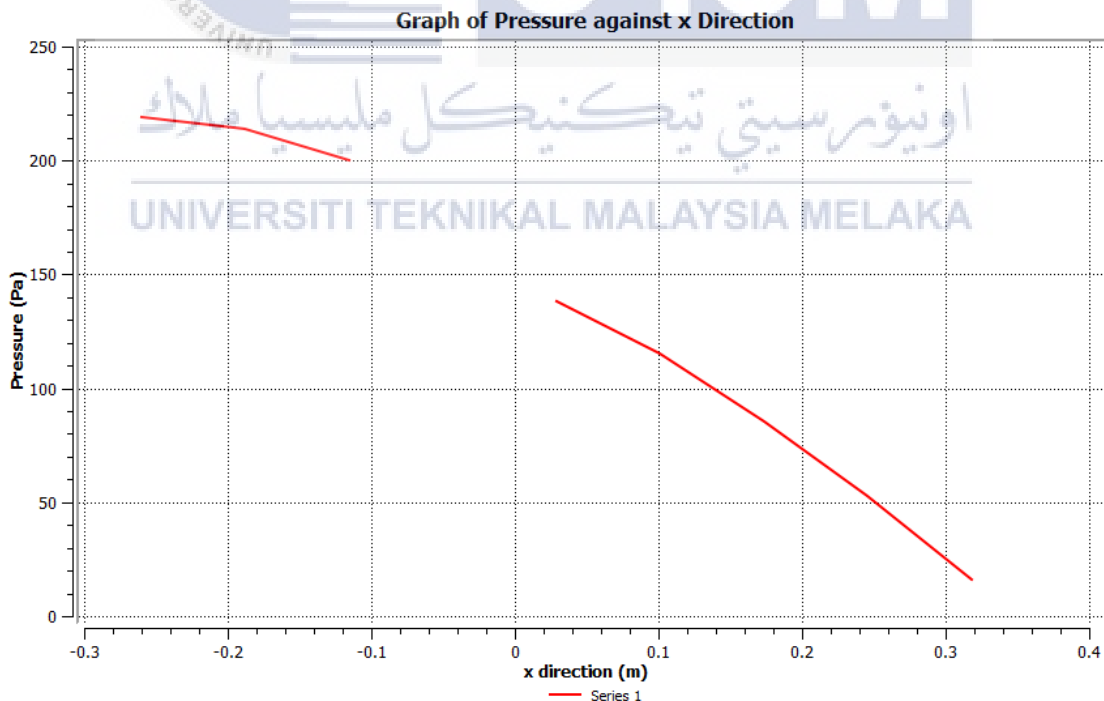


Figure 4.6: Graph of pressure against x direction

Figure 4.7 shows the graph of pressure against time steps at surface monitoring point, point-52. At the beginning of the cycle starts, there pressure reaches approximately 300 Pa due to overshoot and it reaches 218.88 Pa when it starts to be steady. The flow inside the thermoacoustic system is a second-order or higher system. Therefore, second-order or higher order solver scheme can provide more accurate data.

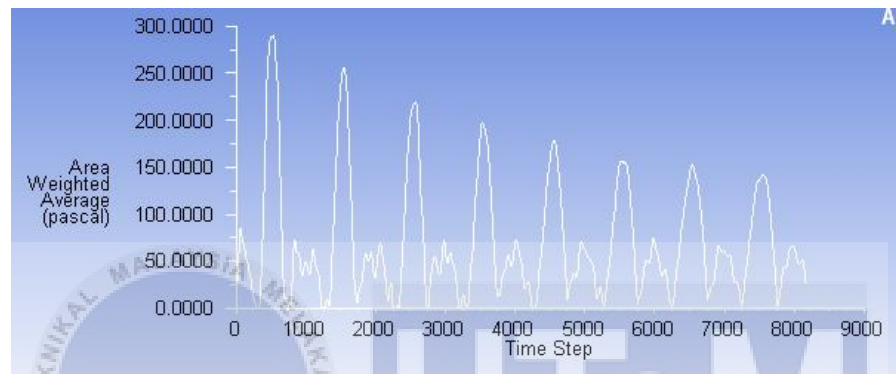


Figure 4.7: Graph of pressure against time step at point-52

4.2.4 Temperature Result

In this section, the temperature across x direction and the particular temperature at points that is located at both ends of the acrylonitrile butadiene styrene (ABS) stack are discussed. The temperature data is captured at the time step of 8,524. Figure 4.8, Figure 4.9, and Table 4.2 show the temperature contour result from computational fluid dynamics (CFD) simulation, graph of temperature against x direction, and average temperature at both end points of ABS stack respectively.

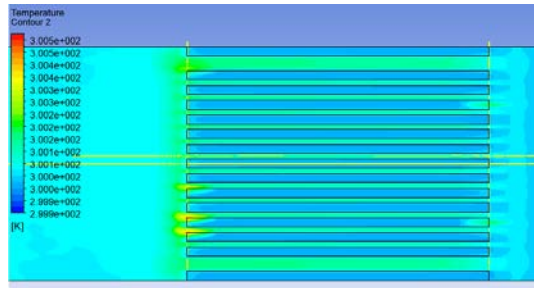


Figure 4.8: Temperature contour result from CFD simulation

Referring to Figure 4.9, the environment temperature for the fluid is 300 K. As the acoustic wave passes through the stack, there is a visible temperature increment at the other end of the stack. The effect of temperature drops is not strong due to parameters which was not optimized, unsteady state of flow, and low drive ratio. Along the x direction, there is a temperature increment from inlet boundary to wall boundary from 299.01 K to 300.07 K.

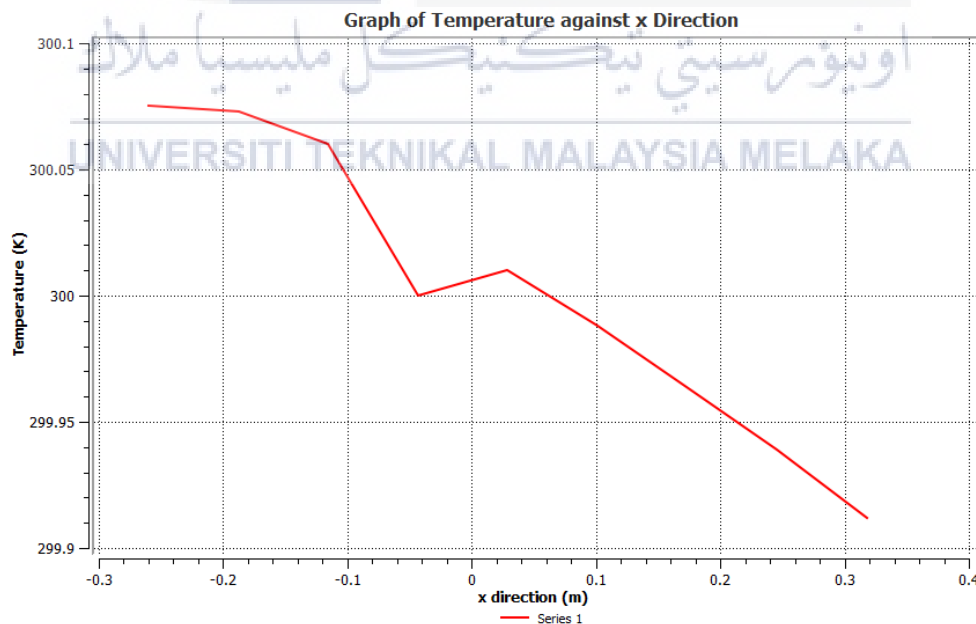


Figure 4.9: Graph of temperature against x direction

Two points as named as point 1 and point 2 are created in the Cartesian coordinate of (-0.02, 0.000975) and (-0.06, 0.000975) in meter. The points are at the two points of stack ends near the gap. Although the temperature differences recorded is 1 K and the acoustic effect is not strong, but this shows that the principle of thermoacoustic is feasible as there is temperature different observed at the two ends of the stack and similar observation was also gained from experimental result as reported earlier in section 4.1.1 where a temperature drop of approximately 1 °C was recorded.

Table 4.2: Average temperature at both end points of ABS stack

Probe	Average Temperature (K)
Point 1 (-0.02, 0.000975)	301
Point 1 (-0.06, 0.000975)	302

4.2.5 Velocity Result

Figure 4.10 and Figure 4.11 show the velocity contour along the resonator that was obtained from computational fluid dynamics (CFD) simulation and the graph of the velocity against x direction respectively. The contour was captured at time steps of 9,250 where the velocity at point-52 reaches maximum.

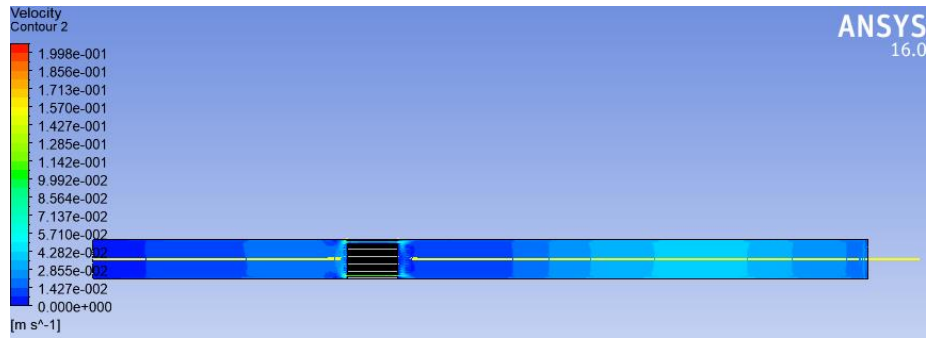


Figure 4.10: Velocity contour result from CFD simulation

The wave particles at each of the points along the x -direction vibrate in sinusoidal patterns as was shown earlier in Figure 4.4. However, as particles move from inlet boundary to the wall boundary at the hard end of the resonator, the amplitude of velocity of the wave particles decreases as it gets closer to the hard end of the resonator following the standing wave criterion. Figure 4.12 shows the sinusoidal change of velocity with respect to time at point-52.



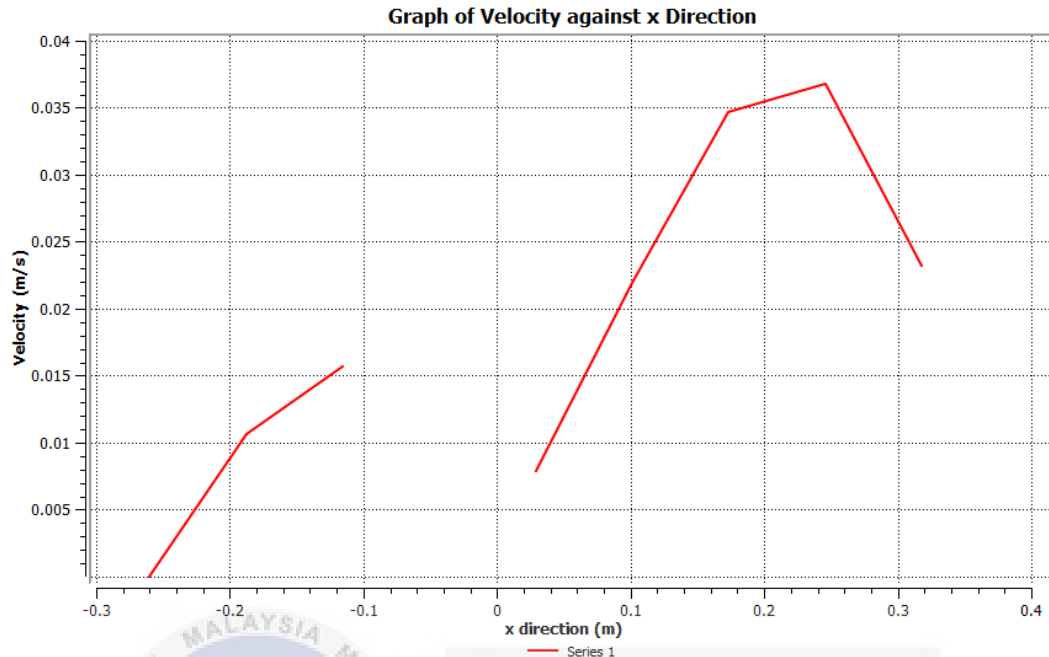


Figure 4.11: Graph of velocity against x direction

Hence, it is observable that the velocity of the air particles along x direction is decreasing from inlet boundary and hit zero at the hard end of the resonator while the air particles in each point along the x direction before reaching the hard end vibrate at their amplitude along their orientation line.

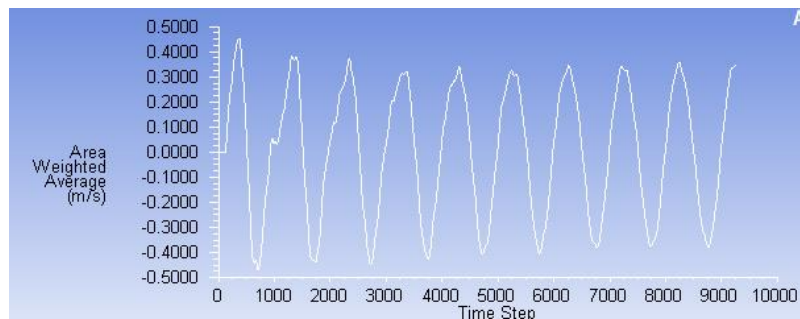


Figure 4.12: Velocity against number of time steps at point-52

4.3 Discussion

In this project, the three-dimensional (3D) CFD simulation for 3D-printed acrylonitrile butadiene styrene (ABS) stack and the porous medium CFD simulation for stainless-steel scrubber stack have failed to generate the results due to meshing problems and inappropriate setup respectively. Firstly, the 3D-printed ABS size is small compared to the size of the resonator that is functioning under 133.45 Hz with 0.65 m length. The quality of the 3D-printed ABS mesh and the resonator is unsolved, and the mesh quality is too poor to proceed the setup. Next, the porous medium CFD simulation for stainless-steel scrubber stack's setup was found to be inappropriate to provide a valid result due to the unidentified porosity and thermal properties of the stainless-steel scrubber stack since the material is came from manufacturer without specification details.

Table 4.3 shows the summary of the simulation cases that have been done throughout the whole final year project (FYP) 2. Fortunately, the 2D CFD simulation on ABS stack thermoacoustic model is successfully built and the data can be obtained.

Table 4.3: Summary of Simulation Cases

CFD Simulation Cases	Reason	Result
3D Porous Medium Stack Simulation	Invalid or inappropriate setup in ANSYS solver setting. Result obtained is invalid.	Fail
3D ABS Stack Simulation	Complicated meshing problem is unsolved due to limited time for research.	Fail
2D ABS Stack Simulation	Result is valid when compared to calculation and experiment result.	Success

Since there is only temperature data obtain from experiment as described in subsection 4.1, the temperature difference across the both ends of the stack and the temperature contour results are discussed by comparing the temperature drops and temperature difference across the stack ends while for other results, the discussion is done at their respective subsection. From experimental result, it is shown that the temperature difference at the both ends of the ABS stack is 0.9 °C as described in subsection 4.1 while for CFD simulation the temperature difference at the both ends of ABS stack is 1 °C.

However, the reading from the experiment is taken when the apparatus has operated for 30 minutes while the CFD simulation reading is taken at 0.064 s of actual flow time. Moreover, the convergence value of the CFD model is at 1×10^{-1} which is loosely converged and this might be one of the reason of data is different than expected (experimental and calculation). Either experiment or simulation, the temperature drops recorded is 1 °C and this effect is not strong enough for generating sufficient cooling effect. This happens presumably due to operating conditions which were not optimized in both the experiments as well as in simulations. Nevertheless, there is temperature drops in the thermoacoustic model and this proves that the thermoacoustic principle is actually working and feasible.

CHAPTER 5

CONCLUSION AND RECOMMENDATION

5.1 Conclusion

As a conclusion, all the objectives as stated in section 1.3 of this Final Year Project (FYP) were achieved. The first objective was achieved based on the description given in Chapter 3 (Methodology). An experimental apparatus of small thermoacoustic refrigerator (TAR) rig was built and the temperature across the two ends of different stacks were measured. The parameters of TAR rig were mostly based on Zolpakar et al. (2016) optimized parameters and their characteristics. Two stacks which are the three-dimensional (3D) printed acrylonitrile butadiene styrene (ABS) stack and the stainless-steel scrubber stack are used in this TAR experiment and their parameters were described in Table 3.5 and Table 3.6, respectively. The results were described in Chapter 4 (Results and Discussion).

Next, the second objective is achieved through the results as shown in subsection 4.1. A temperature drops of approximately 1 °C was obtained in both experimental and simulation works for the 3D-printed ABS stack.

Finally, the third objective is achieved through the description given in subsection 3.3 and the results were as shown in subsection 4.2. The verification of the results for the third objective was as described in subsection 4.2.2 and the results of pressure, temperature, and velocity were obtained and discussed in subsections 4.2.3 to 4.2.5.

In general, a small thermoacoustic effect was observed. The small value of temperature difference that was measured and simulated as described in section 4 was due to the small input of voltage that was supplied to the loudspeaker. In additions, stack parameters were not fully optimized and there was poor insulation in resonator environment. Furthermore, resonance frequency was not measured, and frequency may not be high enough to create sufficient cooling effect. Based on published data, the temperature difference across both ends of the stack provided a stronger thermoacoustic cooling effect and the impact can be seen if the operating condition is set to a fully optimized condition. Although the optimized condition was not achieved but the results that were shown in this project had proven that the thermoacoustic principle was feasible.

UNIVERSITI TEKNIKAL MALAYSIA MELAKA

5.2 Recommendation

Considering the further studies in the flow of a thermoacoustic system, there are few suggestions to be considered in order to create a more efficient thermoacoustic refrigerator (TAR) which can create higher temperature drops at the cold end of the stack. Firstly, the input voltage of the loudspeaker should be increased, or the type of loudspeaker can be changed so that it can produce enough acoustic power for the thermoacoustic cooling effect.

Next, resonance frequency in the resonator should be properly measured measuring the pressure antinode in order to allow the resonator to operate under a resonance condition and produces high acoustic power.

For the computational fluid dynamics (CFD) simulation, it is recommended that the simulation to be solved for three-dimensional (3D) mode instead of two-dimensional (2D) mode. There are few updates that have been done by ANSYS on CFD simulation software, there are new functions and models like acoustic wave models such as “Non Reflecting”, “Impedance” and “Transparent Flow Forcing”. These acoustic wave models might be suitable for certain case studies in thermoacoustic field. It is also advisable to run the simulation for longer time or higher number of time steps so that the results obtained from the simulation are the result of flow when it reaches steady oscillatory state.

Other than CFD simulation, there are few other methods that can be used for the investigation of thermoacoustic system such as DeltaEC, genetic algorithm (GA) analysis, and so on. These methods have been used by some researchers in order to obtain the optimized operating condition for the thermoacoustic system.

Further investigation using these methods are also need. Another suggestion is that the operating frequency of the thermoacoustic refrigerator apparatus can be changed into higher frequency with shorter resonator length in order to increase the velocity amplitude of the air particles in the resonator. Besides, the type of stack can be changed to Mylar, Celcor, and RVC in order to obtain stronger acoustic power.



REFERENCES

Abakr, Y. A. & Chen, B. (2011). The Influence of Wave Patterns and Frequency on Thermoacoustic Cooling Effect. *Journal of Engineering Science and Technology*. 6(3), 392-396.

Acrylic Lucky Draw Box c/w Key. (2018). Retrived from <https://thestationeryshop.com.sg/shop/display-and-presentation/display-andpresentation-acrylic-stand/acrylic-lucky-draw-box-cw-key/>

Advantages of computational fluid dynamics. (2014). Retrieved from <http://www.pretechnologies.com/services/computational-fluid-dynamics/advantage>.

Bhavya, R. (2013). thermoacoustic refrigeration. Retrieved from: https://www.slideshare.net/bhv_r/tar-20186393.

CAST ACRYLIC TUBING 2.375" OD X .250" WALL THICKNESS (SOLD PER FOOT). (2018). Retrieved from <https://www.eplastics.com/Plastic/plexiglass-cast-acrylictubing/ACRCAT2-375ODX-250>

Chin, J. Y. (2017). The Effect of Flow Frequency on Heat Exchanger Used in Thermoacoustics. Universiti Teknikal Malaysia Melaka, Melaka, Malaysia. 46

Cimbala, J. M. & Cengel, Y. A. (2008). Essentials of Fluid Mechanics: Fundamentals and Applications. The McGraw-Hill Companies, Inc.

Desai, A., Desai, K.P., Naik, H.B. & Atrey, M.D. (2017). Optimization of thermoacoustic engine driven thermoacoustic refrigerator using response surface methodology. IOP Conference Series: Materials Science and Engineering. IOP Publishing.

Dhuley, R. C. & Atrey, M. D. (2010) 'Design Guidelines For a Thermoacoustic Refrigerator', Indian Journal of Cryogenics, 35(1-4), pp. 1-6.

Dyatkina, H. S., Achmadin, W. N., Murti, P., Setiawan, I. & Utomo, A. B. S. (2015). Development of the Thermoacoustic Refrigerator System Using a Stack made of some Stainless Steel Mesh and a Hot Heat Exchanger. Indonesian Journal of Physics, 26(01). 5 - 8.

Engineering ToolBox. (2005). Thermoplastics – Physical Properties. Retrieved from https://www.engineeringtoolbox.com/physical-properties-thermoplastics-d_808.html.

Ferris, D. (2018). The Thermoacoustic Engine, Explained. Retrieved from:
<http://theferrisfiles.com/2009/12/the-thermoacoustic-engine-explained/>.

FLP-MT1201. (n. d.). Retrieved from <http://flepcher.com/flpdf/MT1201.pdf>.

Hofler, T. J. (1989). Thermoacoustic Refrigerator Design and Performance. Doctor Philosophy, Physics department, University of California at San Diego..

Hyundai i10 Front Door Speakers Pioneer car speakers 300W. (2018). Retrieved from
<https://www.amazon.co.uk/Hyundai-Front-Speakers-Pioneerspeakers/dp/B00JEWMV TI>.

Ibrahim, A., Arafa, N. & Khalil, E., (2011). Geometrical optimization of thermoacoustic heat engines. In: Proceedings of the Forty-ninth AIAA Aerospace Sciences Meeting including the New Horizons Forum and Aerospace Exposition.

JFE Steel Corporation. (n. d.). JFE Stainless Steel. Retrieved from
<http://www.jfesteel.co.jp/en/products/stainless/catalog/g1e-001.pdf>.

Jinshah, B. S., Ajith, K. R. & Sandeep, V. S. (2013). Study on a Standing Wave Thermoacoustic Refrigerator Made of Readily Available Materials. International Journal of Scientific and Research Publications, 3(7), 1-30.

Mohd Saat, F. A. Z. & Jaworski, A. J. (2013). Oscillatory Flow and Heat Transfer Within Parallel-plate Heat Exchangers of Thermoacoustic Systems. Proceeding of the World Congresson Engineering III.

Newman, J., Cariste, B., Queiruga, A., Davis, I., Plotnick, B., Gordon, M. & Martin, S. S. (2006). Thermoacoustic Refrigeration. GSET Research Journal 2006, 1-8.

Nidhin, T.V. (2016). THERMO ACOUSTIC REFRIGERATION. Retrieved from: <http://talk4technology.blogspot.com/2016/07/thermo-acoustic-refrigeration.html>.

Overview of materials for Acrylic, Cast. (2018). Retrieved from <http://www.matweb.com/search/datasheet.aspx?bassnum=O1303&ckck=1>.

Piccolo, A. (2011). Numerical Computation for Parallel Plate Thermoacoustic Heat Exchangers in Standing Wave Oscillatory Flow. International Journal of Heat and Mass Transfer, 51 (21-22), 4518-4530.

Poese, M. E., Smith R. W. M., Garrett, S. L., Gerwen, R. V. & Gosselin, P. (2004). Thermoacoustic refrigeration for ice cream sales. 6th Gustav Loerentzen Natural Working Fluids Conference, pp. 1-8.

Rosli, N. A., Hasan, R., Alkahari, M. R. & Tokoroyama, T. (2017, November 17). Effect of process parameters on the geometrical quality of ABS polymer lattice structure. Proceedings of SAKURA Symposium on Mechanical Science and Engineering 2017, pp. 3-5.

Rott, N. (1980). Thermoacoustic. *Adv. Appl. Mech.*, 20:135-175.

Russell, D. A. & Weibull, P. (2002). Tabletop thermoacoustic refrigerator for demonstrations. 2002 American Association of Physics Teachers, 70(12). 1231 – 1233. doi: 10.1119/1.1485720.

Scaling (Grid Independence) Test. (2016). Retrieved from <http://www.edsl.myzen.co.uk/downloads/misc/3D%20CFD%20Scaling%20Grid%20Independence%20Test.pdf>

Sharify, E. M., Takahashi, S. & Hasegawa, S. (2016). Development of a CFD model for simulation of a travelling-wave thermoacoustic engine using an impedance matching boundary condition. *Applied Thermal Engineering*, 8 – 10. doi: <http://dx.doi.org/10.1016/j.applthermaleng.2016.07.028>.

Shi, L., Yu., Z. & Jaworski, A. J. (2010). Vortex Shedding Flow Patterns and Their Transitions in Oscillatory Flows Past Parallel-plate Thermoacoustic Stacks. *Experimental Thermal and Fluid Science*, 34(7), 954-965.

SG1005 – digital function signal generator. (2018). Retrieved from https://mcpsh.en.alibaba.com/product/287091019-212404941/SG1005_digital_function_signal_generator.html.

Support: 3D printers. (2017). Retrieved from <https://www.3dsystems.com/shop/support/cubepro/faq>.

Swift, G. (2001). Thermoacoustics: A unifying perspective for some engines and refrigerators. *Zhurnal Eksperimental'noi i Teoreticheskoi Fiziki (Fifth Draft)*. Los Alamos National Laboratory.

Simple Stirling Engine. (n. d.). Retrieved from:
<https://www.webcomsknkwrks.com/schmstirl.jpg>.

Thermo Acoustic Engine. (2018). Retrieved from
<https://www.gyroscope.com/d.asp?product=ACOUSTIC>.

Tijani, M. E. H. (2001). Loudspeaker-driven thermos-acoustic refrigeration. Ph. D. thesis. University of Eindhoven, Netherlands.

Tijani, M. E. H., Zeegers, J. C. H. & Waele, A. T. A. M. (2002). Design of Thermoacoustic Refrigerators. *Cryogenics*, 42, 49-57.

Urieli, I. (n. d.). Chapter 2a – Alpha Stirling Engines. Retrieved from:
<https://www.ohio.edu/mechanical/stirling/engines/engines.html>.

V-Tech Acetic Silicone/ All Purpose Sealant/ Versatile Sealant (Indoor/Outdoor). (2018). Retrieved from [https://shopee.com.my/V-tech-Acetic-silicone-All-purpose-sealantVersatile-sealant-\(Indoor-Outdoor\)-i.13517183.347249048](https://shopee.com.my/V-tech-Acetic-silicone-All-purpose-sealantVersatile-sealant-(Indoor-Outdoor)-i.13517183.347249048).

Yap, M. P. & Cruz, E. D. (2015). Design and Construction of a Simple Standing Wave Thermoacoustic Refrigerator. DLSU Research Congress, 3. 1 – 6.

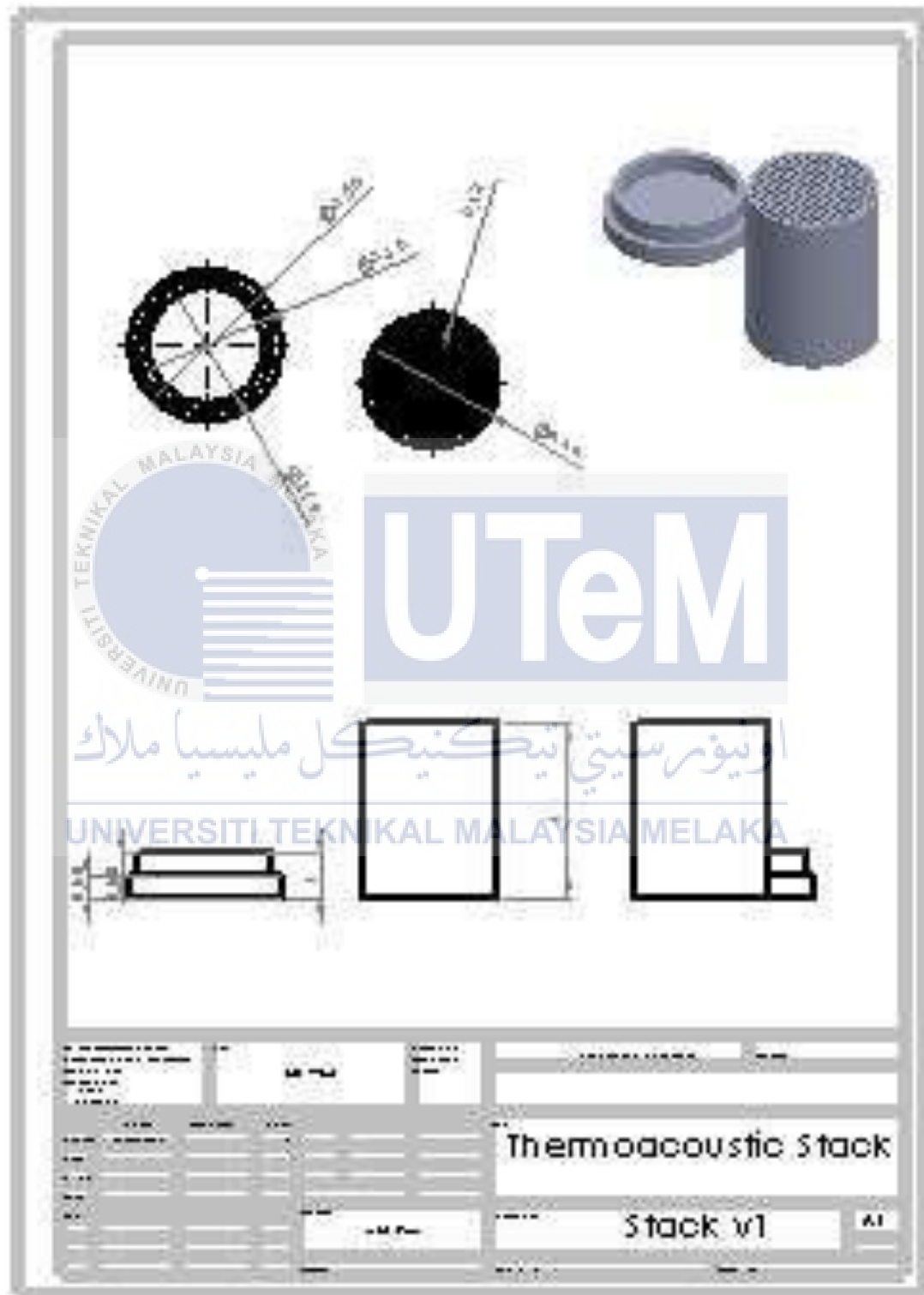
Zolpakar, N. A., Mohd-Ghazali, N. & Ahmad, R. (2014). Analysis of increasing the optimized parameters in improving the performance of a thermoacoustic refrigerator. Energy Procedia, 61, pp. 33-36. doi: 10.1016/j.egypro.2014.11.899.

Zolpakar, N. A., Mohd-Ghazali, N. & Ahmad, R. (2016). Single-Objective Optimization of a Thermoacoustic Refrigerator. Applied Mechanics and Materials, 819, pp. 88-93. doi: 10.4028/www.scientific.net/AMM.819.88.

Zolpakar, N. A., Mohd-Ghazali, N. & Hassan, E. F. M. (2016). Performance analysis of the standing wave thermoacoustic refrigerator: A review. Renewable and Sustainable Energy Reviews. Elsevier, 54, pp. 626-634. doi: 10.1016/j.rser.2015.10.018.

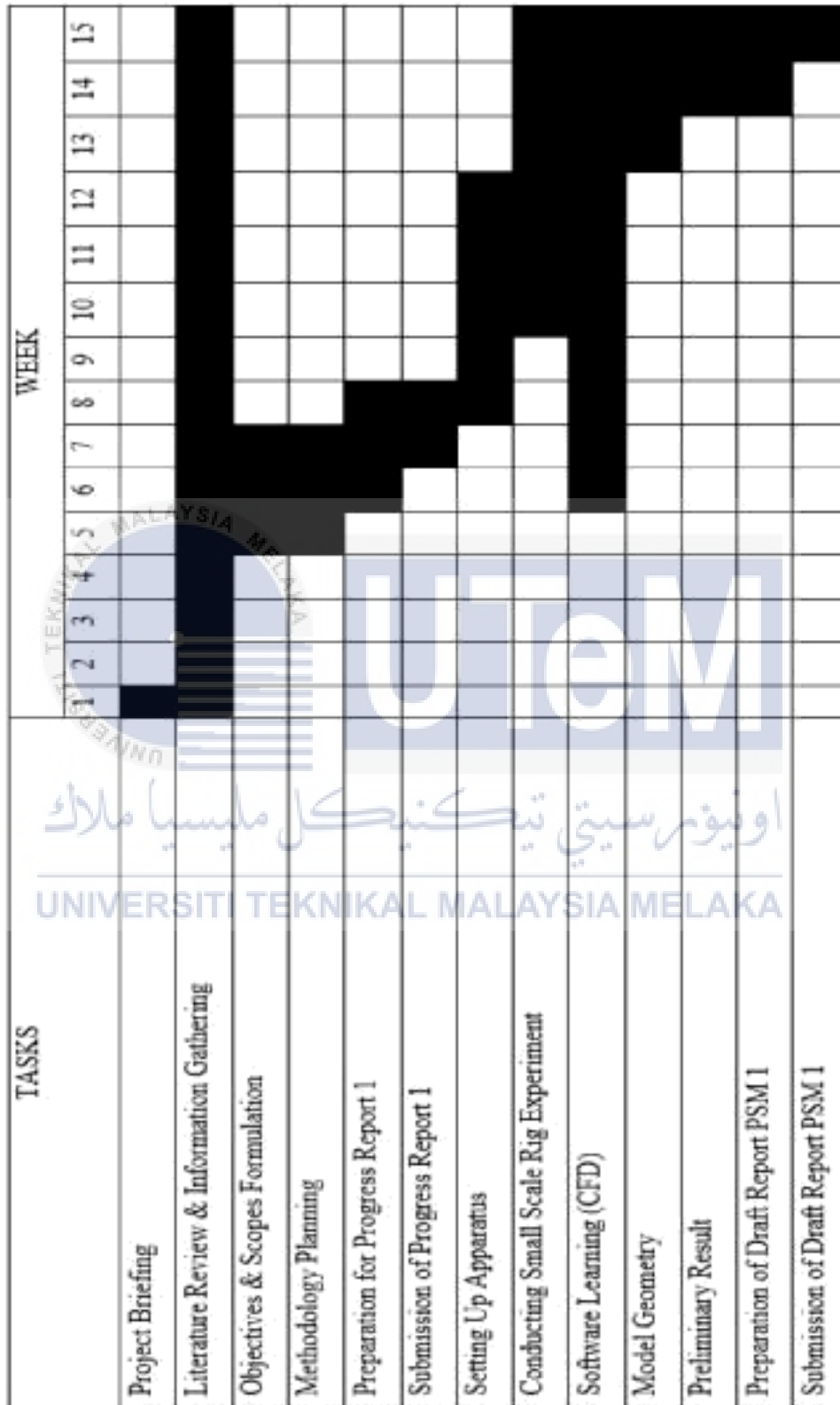
Zolpakar, N. A., Mohd-Ghazali, N., Ahmad, R., Maréc , T. (2017). Performance of a 3Dprinted stack in a standing wave thermoacoustic refrigerator. The 8th International Conference on Applied Energy – ICAE2016. 1382 – 1387. doi: 10.1016/j.egypro.2017.03.513.

APPENDIX A1 Drawing of ABS Stack



APPENDIX A2 Gantt Chart for PSM 1

Gantt Chart for PSM 1



APPENDIX A3 Gantt Chart for PSM 2

